

Fermi bubbles: the collimated outburst needed to explain forward-shock edges

Santanu Mondal,^{1*} Uri Keshet,^{1†} Kartick C. Sarkar,^{2‡} and Ilya Gurwich³

¹ *Physics Department, Ben-Gurion University of the Negev, POB 653, Be'er-Sheva 84105, Israel*

² *Center for Astrophysics and Planetary Science, Racah Institute of Physics, The Hebrew University of Jerusalem, Israel*

³ *Department of Physics, NRCN, POB 9001, Beer-Sheva 84190, Israel*

Accepted XXX. Received YYY; in original form ZZZ

ABSTRACT

The bipolar, nonthermal, high-latitude lobes known as the Fermi bubbles (FBs) are thought to originate from a massive energy release near the Galactic centre (GC). We constrain the FB engine and the circumgalactic medium (CGM) by analytically and numerically modeling the FB edges as strong forward shocks, as inferred from recent observations. A non-directed energy release produces shocks too spherical to account for observations even for a maximally massive Galactic disc, critical CGM rotation, or injection effectively offset from the GC. In contrast, collimated injection nearly perpendicular to the disc can account for observations in both ballistic (free expansion) and slowdown regimes, as we show using a simple stratified evolution model verified by hydrodynamic simulations. FBs still in their ballistic regime require injection (at $z \simeq 100$ pc heights in our model) with a half-opening angle $\theta \simeq 4^\circ$, a normalized velocity $\beta_{-2} \equiv v/(0.01c) \gtrsim 0.4$, and an energy $E \gtrsim 2\beta_{-2}^2 \times 10^{55}$ erg, launched $T \simeq 3.3\beta_{-2}^{-1}$ Myr ago, showing a distinctive low-pressure region behind the bubble head. Slowing-down (mass accumulated) FBs require a faster injection, a thinner jet, a smaller $E/(\beta_{-2}\theta)^2$, and a comparable T , and follow a ballistic stage that must reach a height $z_s \gtrsim 5$ kpc.

Key words: ISM: jets and outflows – Galaxy: centre – Galaxy: halo

1 INTRODUCTION

The Fermi bubbles (FBs) are bipolar, non-thermal lobes, extending to latitudes $|b| \simeq 50^\circ$ – 55° above and below the Galactic centre (GC). Their high-latitude signature was first revealed in γ -rays, by the *Fermi* Gamma-ray Space Telescope (Dobler et al. 2010; Su et al. 2010, henceforth S10), but subsequently also in microwaves (Dobler & Finkbeiner 2008; Dobler 2012; Planck Collaboration 2013) and in X-rays (Keshet & Gurwich 2018, hereafter KG18). The edges of the FBs are distinct and easily traced (Keshet & Gurwich 2017, hereafter KG17), linking them to large (Sofue 2000), intermediate (Bland-Hawthorn & Cohen 2003) and small (Baganoff et al. 2003) scale (Sofue 2000; Bland-Hawthorn & Cohen 2003) nonthermal features, and thus identifying the FBs as arising from a major, $\geq 10^{55}$ erg event (Veilleux et al. 2005, and references therein) near the GC.

The origin of the FBs is still uncertain, present models including a starburst (Carretti et al. 2013; Lacki 2014;

Sarkar et al. 2015b, hereafter S15b), an SMBH jet (Cheng et al. 2011; Guo & Mathews 2012; Zubovas & Nayakshin 2012), SMBH accretion wind (Mou et al. 2014, 2015), or steady star formation (Crocker 2012). Due to their dynamical, nonthermal nature, and the vast energy involved, an accurate interpretation of the FBs is important for understanding the energy budget, structure, and history of our Galaxy.

Correctly interpreting the FBs is important for understanding additional, possibly related phenomena, such as ‘chimneys’ which may play a role in the transport of energy to the base of the FBs (Ponti et al. 2019), symmetric lobes on a few 100 pc scales (Heywood et al. 2019), and magellanic echoes (Bland-Hawthorn et al. 2019), where two bipolar ionization radiation cones are associated with the GC took place ~ 3.5 Myr ago. Recent UV absorption survey of quasar sightlines passing through the FBs have been used to map the kinematics of associated cold clouds. The velocity of the clouds are symmetric in both hemispheres, decreases from ~ 900 km s⁻¹ at low latitude to ~ 350 km s⁻¹ at high latitudes (Fox et al. 2015; Bordoloi et al. 2017; Karim et al. 2018; Ashley et al. 2020).

In spite of their dramatic appearance in the γ -ray sky,

* E-mail: santanu@post.bgu.ac.il

† E-mail: ukeshet@bgu.ac.il

‡ E-mail: sarkar.kartick@mail.huji.ac.il

even the nature of the FB edges is not widely agreed upon. Previous models have interpreted the FB edge as either an outgoing shock (Fujita et al. 2013), or a termination shock of a wind (Lacki 2014), or a discontinuity (Crocker 2012, S15b). More recent studies provided evidence that the edges are forward shocks. This evidence is based on the little variation of the γ -ray spectrum with position along the edge, indicating a strong, Mach $M > 5$ shock (KG17), on a faint X-ray shell inside the FB edges found by stacking *ROSAT* data and consistent with $M > 4$ forward shocks (KG18), and on a combined analysis of the microwave and γ -ray spectrum (Keshet & Gurwich, in preparation). These claims are, however, in tension with some other results (Kataoka et al. 2013; Carretti et al. 2013; Kataoka et al. 2021).

The identification of the FB edges as strong forward shocks simplifies, in a sense, their analysis, because their supersonic motion renders them less sensitive to details of the energy release and CGM properties than the alternative, discontinuity or reverse shock models. We thus use hydrodynamic simulations to study which properties of the FB engine and of the CGM are consistent with the observed morphology of the FBs. In particular, we use the edges identified by applying gradient filters to the *Fermi* data (KG17), and the projection of the toy model for the FBs in 3D (KG18).

The paper is organised as follows. In §2, we describe the methodology and the numerical setup. The analysis of putative FBs generated by an isotropic, non-directed injection of energy is presented in §3, and shown to yield bubbles too wide to be consistent with the FBs. In §4, we study FBs generated by the collimated injection of both momentum and energy, presenting a stratified evolution model in §4.1 and the corresponding simulations in §4.2. Our results are summarised and discussed in §5. We present the Galactic model implemented in the simulations in §A, and representative convergence tests in §B.

2 METHOD

We simulate a simple numerical model of the Galaxy, inject energy and in some cases also momentum rapidly near the Galactic centre, and examine the resulting, evolved FBs with an emphasis on the robustly-measured geometry of the expanding, forward shock. The parameters of the Galactic model and of the injecting engine are varied, to quantify the dependence of the observed quantities upon the assumptions, and to identify the physical condition which could account for the observed FB edges.

The analysis is based on hydrodynamic simulations using the publicly available Eulerian grid code PLUTO-v4.0 (Mignone et al. 2007). The simulations are axisymmetric and non-relativistic, modeling a viscous fluid with no heat conduction, with an ideal gas of polytropic index $\gamma = 5/3$, without cosmic-rays, and with a mean particle mass $\mu_m m_p$, where m_p is the proton mass and $\mu_m \simeq 0.6$. These assumptions are reasonable for the present problem, as we focus mainly on the geometry of the shock, at \gtrsim kpc scales. Spherical coordinates (r, θ, ϕ) centered on the GC are used, with polar coordinate $\theta = \pi/2$ along the Galactic disc and a frozen azimuthal coordinate ϕ . The computation box extends from r_0 to 15 kpc in the radial direction and from $\theta = 0$ to $\pi/2$ in the polar direction. The inner boundary in

Table 1. Fixed CGM parameters. Additional CGM parameters varied among simulations are provided in Table 2 and Table 3.

Parameter	Definition	Value
$M_{\text{vir}} [M_{\odot}]$	Virial mass	1.2×10^{12}
$r_{\text{vir}} [\text{kpc}]$	Virial radius	250
$d [\text{kpc}]$	DM core radius	6.0
$r_s [\text{kpc}]$	Scale radius	20.8
$c_{\text{vir}} = r_{\text{vir}}/r_s$	Concentration parameter	12
$a_d [\text{kpc}]$	Disc scale length	3.0
$b_d [\text{kpc}]$	Disc scale height	0.4
$a_b [\text{kpc}]$	Bulge scale radius	2.0
$\rho_{d0} [m_p \text{ cm}^{-3}]$	Disc mass density	1.0
$\rho_{h0} [m_p \text{ cm}^{-3}]$	Halo mass density	0.019
$T_d [\text{K}]$	Disc temperature	4×10^4
$T_h [\text{K}]$	Halo temperature	2×10^6
$T_{\text{cmz}} [\text{K}]$	CMZ temperature	10^3
f_d	Disc gas rotation	0.975
f_{cmz}	CMZ rotation	0.0
$r_{\text{max}} [\text{kpc}]$	Outer boundary of the box	15
$r_{\text{gd}} [\text{kpc}]$	Sun Galactocentric radius	8.5

the radial direction is set to have the values corresponding to the hydrostatic equilibrium, except where we inject jet energy. The outer boundary in the radial direction is set to have zero gradient. In the polar direction, $\theta = 0$ and $\pi/2$ boundaries are set to be axisymmetric and reflective, respectively. For convenience, we introduce also a cylindrical coordinate system (R, ϕ, z) , centered on the GC with axial coordinate z along $\theta = 0$.

The Galactic model and its numerical setup follow the work of Sarkar et al. (2015a, hereafter S15a), as detailed in §A. The model includes two gas components of the interstellar medium (ISM): a hot, 4×10^4 K, disc-like component and a warm, 2×10^6 K, halo component. The model assumes that the gas components are in hydrostatic equilibrium with the gravity of dark matter, the disc, and the bulge, and each component is initially isothermal. The warm component associated with the disc rotates approximately with the stars; a rotation parameter $f_h \leq 1$ is introduced to quantify the ratio between halo rotation and stellar rotation (see §A). The halo has a global baryon fraction $f_b = 0.16$, consistent with the cosmic value of Ω_b/Ω_m . The fixed parameters of our nominal Galactic model are provided in Table 1. For these parameters, the mass density of the halo — which plays an important role in the bubble evolution — is distributed at large radii as $\rho_h \simeq 4.4 \times 10^{-4} (r/10 \text{ kpc})^{-1.5} m_p \text{ cm}^{-3}$. Galactic model parameters that are varied among simulations are provided in Table 2 for non-directed bubble simulations, and in Table 3 for jetted bubble simulations.

We consider two different modes of FB engines, operating over a short, \ll Myr timescale near the GC, as illustrated in Figure 1: energy only (henceforth: non-directed) or both energy and momentum (henceforth: jetted) injection. The non-directed mode can arise, for example, from starburst activity at some distance from the GC, or from a dissipated jet at some height above the GC, so we consider such injection both close to the GC (around r_0 ; henceforth GC injection) and at intermediate latitudes (around $r \sim$ kpc; IL injection). Jetted emission can arise from a relativistic jet launched from the central black hole (CBH) in the GC, and is represented for simplicity as simultaneous energy and momentum in the $\theta = 0$ direction, injected at r_0 . As we show below, jetted injection can lead to two dif-

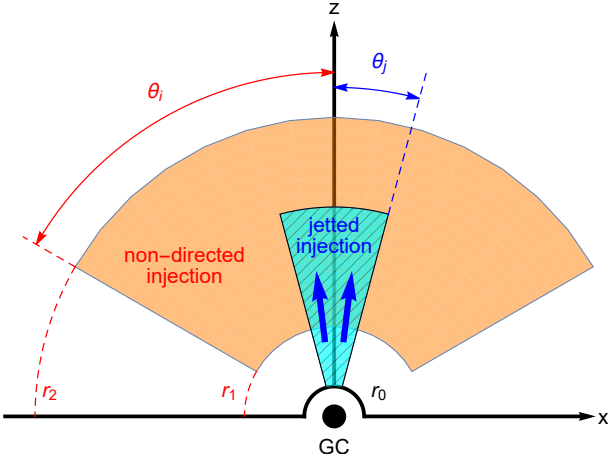


Figure 1. Illustration of non-directed (orange shaded region) and jetted (hatched cyan, with arrows showing the momentum direction) injection is based on our simulated FBs.

ferent types of FBs: ballistic bubbles for high energies, and slowing-down, non-ballistic for low energies.

We detail the two (GC and IL) non-directed modes in §2.1, and the two (ballistic and slowdown) jetted modes in §2.2. Shear in the flow, especially during the injection of slowdown jetted bubbles, can give rise to substantial Kelvin-Helmholtz instabilities (KHI), which are dealt with in §2.3. The simulation results are finally projected and compared to observations, in a method outlined in §2.4. Convergence tests are provided in §B.

2.1 Non-directed injection

We begin with the simple, non-directed injection of energy with zero momentum, either from the vicinity of the CBH (GC), or from intermediate latitudes (IL). We assume that the injected energy is thermalised within a conical region (with half opening angle θ_i) around the rotation axis of the Galaxy. The injected energy is thus added to the internal energy above the injection point, at some radial range $r_1 < r < r_2$, as illustrated by the orange shaded region in Figure 1. The internal energy is added at a constant rate

$$\dot{e}_j = \frac{E_j}{V_j t_j} \quad (1)$$

during a short time interval time t_j , after which injection is turned off. Here, both the total injected energy E_j and the injection volume

$$V_j = \frac{4\pi}{3}(r_2^3 - r_1^3)(1 - \cos \theta_i) \quad (2)$$

are defined for the full sky, summing both hemispheres.

With the above general setup, we explore the simulated appearance of the FBs for different central engines and Galactic structures, by varying the properties of energy injection and of the Galactic model, as detailed in Table 2. Such variations are essential because, as shown in §3, extreme — and even implausible — choices of the Galactic model parameters are needed in order to produce simulated FBs of any resemblance to the observations.

In particular, we vary the mass of the Galactic disc and of the bulge, which can modify the resulting bubble morphology, while keeping the virial mass of the galaxy fixed. We also vary the rotation frequency of the Galactic components, which affect their structure and therefore also the appearance of the shock. The geometrical parameters of the injection volume have little effect near the GC, but they do have some impact at high latitudes, where we consider in particular a narrow, $\theta_i \simeq 5^\circ$ cone representing a putative dissipated jet.

We find converged results with a minimal resolution of 1024×256 with a stretched¹ grid along the r and θ directions, with no need to introduce viscosity. All of our production runs for the non-directed set-ups have this resolution.

2.2 Jetted injection

Next, consider jetted injection, introducing both energy and momentum in the $\theta \simeq 0$ direction, approximately perpendicular to the Galactic plane. Injection into the computation domain is implemented by modifying the r_0 , inner boundary within the half opening angle θ_j of the jet, introducing a luminosity $L_j = E_j/t_j$ over a short time interval t_j , in the form of kinetic energy due to momentum in the \hat{r} direction. This injection scheme is illustrated by the hatched cyan region in Figure 1. The quantities E_j and L_j , like all extensive injection parameters above and below, pertain to the full sky, *i.e.*, to both hemispheres combined.

The energy injected is predominantly kinetic, so the injected mass is taken as

$$\dot{M}_j = \frac{2L_j}{v_j^2}, \quad (3)$$

where v_j is the non-relativistic velocity of the injected gas; relativistic corrections are omitted. The area of the injection boundary is given by

$$A_j = 4\pi(1 - \cos \theta_j)r_0^2, \quad (4)$$

so the mass density of the jet material injected at r_0 is given by

$$\rho_j = \frac{\dot{M}_j}{A_j v_j}. \quad (5)$$

Kinetic energy is assumed to dominate at the base of the jet, so the thermal energy flux $(\gamma - 1)^{-1} \gamma P v_j$ is taken to be negligible with respect to the kinetic energy flux $(1/2) \rho_j v_j^3$ throughout the injection boundary. Here, P is the gas pressure.

The bubbles formed by jetted injection are not very sensitive to the Galactic model in the ballistic case, and depend mostly on the halo distribution for the slowdown case. The minimum grid necessary for convergence is a 1024×512 uniform grid in the r and θ directions for the ballistic case, and a 1536×768 uniform grid for the slowdown case.

2.3 Overcoming KHI

The emergence of strong shear, in particular for jetted injection, gives rise to KHI that corrugate the discontinuities,

¹ See <http://plutocode.ph.unito.it/files/userguide.pdf> for details.

thus leading to expensive simulations with a short time step and early dissipation of the kinetic energy. We avoid these instabilities, especially at the early stages of jet formation, because details of the early evolution are in any case poorly understood and not well-constrained by observations.

One modification we thus incorporate is smoothing of the injected velocity gradient, by switching from a step function at θ_j to a continuous, linear velocity profile

$$v(r = r_0, \theta < \theta_j; t < t_j) = \left(1 - \frac{\theta}{\theta_j}\right) v_j, \quad (6)$$

in which case the tabulated parameter v_j refers to the maximal, axial velocity. We keep ρ_j uniform, so Equation 5 is replaced by

$$\rho_j = \frac{L_j}{2\pi \left[1 - 6 \frac{\theta_j - \sin(\theta_j)}{\theta_j^3}\right] r_0^2 v_j^3}. \quad (7)$$

More importantly, we incorporate viscosity, modeled for simplicity as the isotropic, dynamic viscosity of a nonmagnetized plasma (Braginskii 1958; Spitzer 1962)

$$\mu \simeq 6 \times 10^3 \left(\frac{\ln \Lambda}{37}\right)^{-1} \left(\frac{T}{10^8 \text{K}}\right)^{5/2} \text{ gm cm}^{-1} \text{ s}^{-1}, \quad (8)$$

where T is the temperature in Kelvin and $\ln \Lambda$ is the Coulomb logarithm. To prevent exceedingly small time steps, we cap the viscosity at $\mu_{\text{max}} = 10 \text{ g cm}^{-1} \text{ s}^{-1}$, which is sufficient for present purposes. Indeed, KHI of wavelengths λ are suppressed by viscosity (*e.g.*, Lamb 1932; Chandrasekhar 1961; Roediger et al. 2013)

$$\mu \gtrsim \frac{\rho \lambda \Delta v}{64 q_\rho^{1/2}}, \quad (9)$$

where Δv is the shear velocity and q_ρ is the density contrast across the discontinuity. If we replace λ with the scale of the bubble at a given time (z), we will have the value necessary to insure KHI suppression at all scales. At small scales, this upper limit keeps increasing as the bubble grows, but beyond $z \gtrsim 0.35 \text{ kpc}$, the density drops rapidly as the bubble grows. At $z \sim 0.35 \text{ kpc}$ our simulation shows that $\rho_d = 0.3 \text{ cm}^{-3}$ and $\rho_h = 2 \times 10^{-3} \text{ cm}^{-3}$ whereas, $\Delta v = 0.1c$ is chosen for our nominal simulation, which gives, $\mu \sim 13 \text{ gm cm}^{-1} \text{ s}^{-1}$ as the necessary threshold to suppress all KHI modes.

2.4 Projection and comparison with observations

In order to compare the simulated bubble to FB observations, we project the simulation box for an observer at the solar position, taken as $(r, \theta, \phi) = (8.5 \text{ kpc}, \pi/2, \pi)$. We use the Projection Analysis Software for Simulations (PASS; S15a), which computes the surface brightness by integrating the emissivity along the line of sight (LOS),

$$F_X(l, b) = \frac{1}{4\pi} \int_{\text{LOS}} n^2 \varepsilon(T, Z) ds, \quad (10)$$

where n is the particle number density and T is the temperature. The emissivity $\varepsilon(T, Z)$ is computed assuming a metallicity $Z = 0.2Z_\odot$ by interpolating the MEKAL from XSPEC (Mewe et al. 1985, 1986; Liedahl et al. 1995; Arnaud & Rothenflug 1985) data; we use the 2.0 – 10.0 keV band, sufficient for our purposes. The LOS is extended beyond

the simulation box, out to $r = 100 \text{ kpc}$, assuming steady-state equilibrium with the background gravitational field, extending the temperature and density profiles of our Galactic model.

Given the projected image of the simulation at a given time t , we identify the bubble edges by applying a gradient filter, of 2° width. The maximal latitude b of the projected bubble, and its maximal longitudinal half width Δl , are then measured as a function of t . The age \mathbb{T} of the bubble is estimated by requiring $b(\mathbb{T}) = 52^\circ$, as inferred from FB observations. The measured bubble edge at this time is compared to the edges inferred by applying a gradient filter to the *Fermi* map (6° width for southeast bubble; KG17) and to the projection of a FB toy model (KG18).

3 NON-DIRECTED INJECTION

We simulate various non-directed injection models, as described in §2.1, and compare the bubbles as they reach $b \simeq 52^\circ$ with the observed FBs. The parameters of select non-directed injection simulations, which are displayed in the following figures, are detailed in Table 2. The table also provides the central measured properties of each simulated bubble: its age \mathbb{T} and maximal half width Δl .

Figure 2 shows the *Fermi*-like bubbles obtained for our nominal GC (S1; top panels) and IL (S2; bottom panels) injection simulations. The figure shows the 2 – 10 keV surface brightness maps (left panels) and the spatial distributions of density and temperature (in cylindrical coordinates; right panels). For comparison with observations, FB edge contours traced by a gradient filter (KG17, red dotted curve) and obtained from projecting a toy model (KG18; solid blue) are superimposed on the surface brightness maps. For this purpose, we adopt the south eastern FB edge, which is better measured than its northern and western counterparts due to the abundance of dust in the northern hemisphere and the elongation of the bubbles to the west.

As the upper panel of Figure 2 shows, our nominal GC injection model produces bubbles with strong forward shocks that are approximately spherical, and quite inconsistent with the more elongated, thinner morphology of the observed FBs. Such quasi-spherical bubbles are expected as the shock propagates far from the GC, into an initial CGM density that itself becomes quasi-spherical at $|z| \gtrsim 1 \text{ kpc}$ distances from the Galactic plane. For injection near the GC, the initial blastwave is close to spherical and accumulates mass rapidly, so the transition from an initial quasi-ballistic propagation into an approximately self-similar propagation occurs relatively quickly. Indeed, after $\sim 0.5 \text{ Myr}$, we find an $R \propto t^{0.6}$ and $z \propto t^{0.6}$ evolution, close to the spherical self-similar $r \propto t^{4/7}$ solution expected for the $\rho_h \propto r^{-3/2}$ radial profile implemented by our Galactic model at large radii. The inner structure of the bubble presents a reverse shock, separated from the forward shock by a deformed contact discontinuity.

As the lower panel of Figure 2 shows, our nominal IL injection model produces forward shocks similar to those of the GC injection, and again far too spherical to account for the FB observations. Such injection, representing for example the dissipation of a jet at some intermediate latitude, avoids the initial propagation of the blastwave through the high

Table 2. Variable parameters for select non-directed injection simulations presented in figures 2–4.

Parameter	Definition	GC Injection					IL Injection				
		S1	S1a	S1b	S1c	S1d	S2	S2a	S2b	S2c	S2d
M_d [$10^{10} M_\odot$]	Disc mass	6	6	12	6	12	6	6	12	6	12
M_b [$10^{10} M_\odot$]	Bulge mass	2	2	2	4	4	2	2	2	4	4
f_h	CGM rotation	0.33	0.9	0.33	0.33	0.9	0.33	0.9	0.33	0.33	0.9
E_j [10^{56} erg]	Injected energy	2					2				
t_j [Myr]	Injection duration	0.01					0.01				
r_1 [kpc]	Minimal injection radius	0.02					1.0				
r_2 [kpc]	Maximal injection radius	0.04					2.0				
θ_i	Injection opening angle	90°					5°				
r_0 [kpc]	Inner boundary	0.02					0.02				
\mathbb{T} [Myr]	Bubble age (approximate)	5	6	2.8	3.5	2.8	4.3	5	2	2.7	1.5
Δl	Bubble half width (approximate)	37°	34°	33°	34°	27°	36°	33°	33°	35°	24°

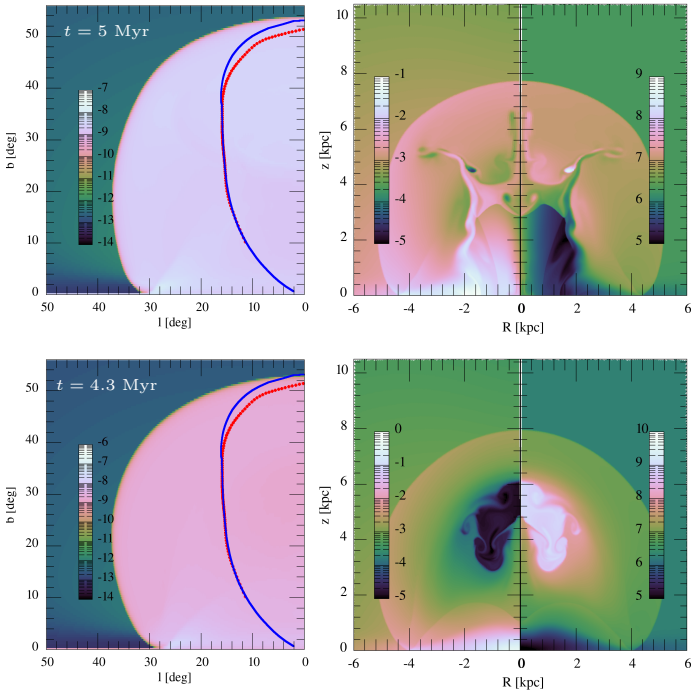


Figure 2. Simulated *Fermi*-like bubbles obtained from our nominal models of injection near the CBH (GC; setup S1 at $t = 5$ Myr; top panels) and at intermediate latitudes (IL; setup S2 at $t = 4$ Myr; bottom panels). Full simulation parameters are listed in Table 1 and Table 2, and snapshot times are provided in the upper left labels. Left panels: projected 2–10 keV surface brightness at the Solar system (F_X [erg s $^{-1}$ cm $^{-2}$ sr $^{-1}$] colorbar), with superimposed FB edges based on a gradient filter (of 6° width for southeast bubble; from KG17; red dotted curve) and on projecting a toy model (KG18; solid blue). Right panels: spatial distributions of the number density (left half; n [cm $^{-3}$] colorbar) and temperature (right; T [K] colorbar) of the CGM. The forward shock presents as the large scale, sharp inward jump in the projected F_X and as the external, sharp jumps in the non-projected n and T .

density regions near the GC, resulting in slightly narrower bubbles. However, the sideways expansion of the shock is rapid, leading to wide bubbles that are still inconsistent with the FBs. Here, it takes slightly more time for the bubbles to settle on a power-law temporal evolution, characterised by a more noticeably sublinear and less spherical, $R \propto t^{0.5}$ and $z \propto t^{0.4}$ growth after ~ 1 Myr. The inner structure

of the bubbles is noticeably different for IL injection, presenting reverse shocks reflected from the Galactic plane at low latitude and a closed contact discontinuity structure at mid-latitudes.

After its ballistic stage, the evolution of the bubbles becomes sensitive to the properties of the CGM distribution. It is therefore natural to ask if there are any plausible modifications to the Galactic model that could alter the simulated bubbles and produce an acceptable match to the observed FBs. As the FBs are substantially thinner than the bubbles in Figure 2, a better fit to the observations requires enhancing the collimation of the simulated bubbles. Such collimation can be established by considering flatter, more disc-like mass distributions near the origin of the bubbles. This, in turn, can be facilitated by a faster CGM rotation, a more massive disc, or a more massive bulge. These three modifications are considered, separately and combined, in Figure 3 for GC injection, and in Figure 4 for IL injection.

In the first three rows of these two figures, we consider a radical modification of a single parameter: (i) a nearly maximal halo rotation parameter, $f_h = 0.9$; (ii) doubling the disc mass, $M_d = 1.2 \times 10^{11} M_\odot$; and (iii) doubling the bulge mass, $M_b = 4 \times 10^{10} M_\odot$. The fourth row simultaneously combines all three modifications, to examine their cumulative effect. The masses of the Galactic stellar components are varied while keeping the dark matter mass of the Galaxy constant; this changes the local gravity near the disc, but does not alter the total mass of the Galaxy (including dark matter) by more than $\sim 10\%$. The effect of changing the gravity translates to a slightly different gas density profile near the disc. A similar effect could also be obtained by varying the temperature profile of each component, but our present construction of the CGM profile does not accommodate a variable temperature.

As the two figures show, these modifications to the CGM model, although extreme, are still insufficient to provide the necessary collimation of the bubbles. This conclusion holds even when all modifications are combined, for both GC and IL injection, and our results are converged and not sensitive to the addition of viscosity. In both injection methods, the modifications do somewhat enhance the collimation, in particular when all modifications are combined with IL injection. However, the resulting bubbles are still too wide and too spherical to account for the observations. The collimation is associated with taller and younger bubbles, reaching $z \simeq 10$ kpc and $\mathbb{T} \sim 1.5$ Myr for the thinnest of the bubbles in the figures. Extrapolation suggests that

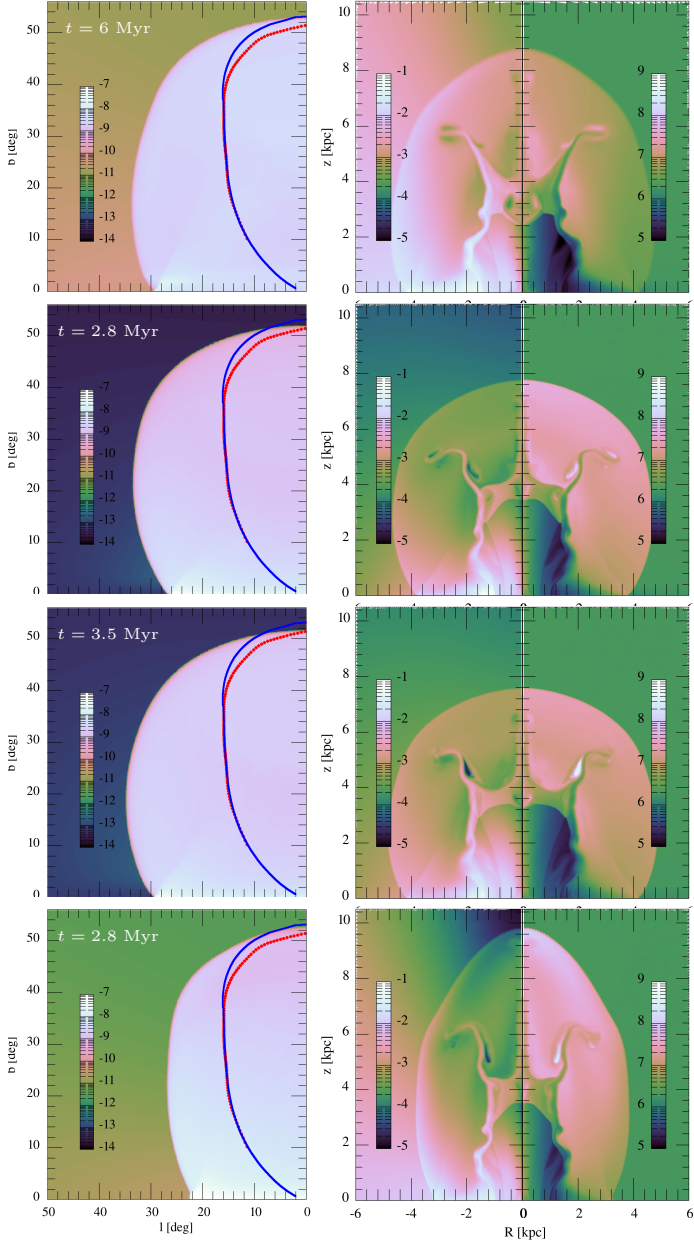


Figure 3. Variations on GC injection: each row is similar to the top row of Figure 2, and uses the same notations, but with some parameter change giving slightly thinner bubbles: nearly maximal halo rotation, $f_h = 0.9$ (first row), double the disc mass, $M_d = 1.2 \times 10^{11} M_\odot$ (second row), double the bulge mass, $M_b = 4 \times 10^{10} M_\odot$ (third row), and all three modifications combined (bottom row). Simulation parameters (setups S1a–d, top to bottom) are provided in the middle columns of Table 2.

a good match to the FB morphology would require unrealistically massive central Galactic components and young bubbles.

We conclude that the rapid injection of energy near the GC, or even at intermediate latitudes above it, cannot explain the morphology of the FBs as forward shocks, for any Galactic model consistent with present observations. Our results are consistent with previous studies Zhang & Guo

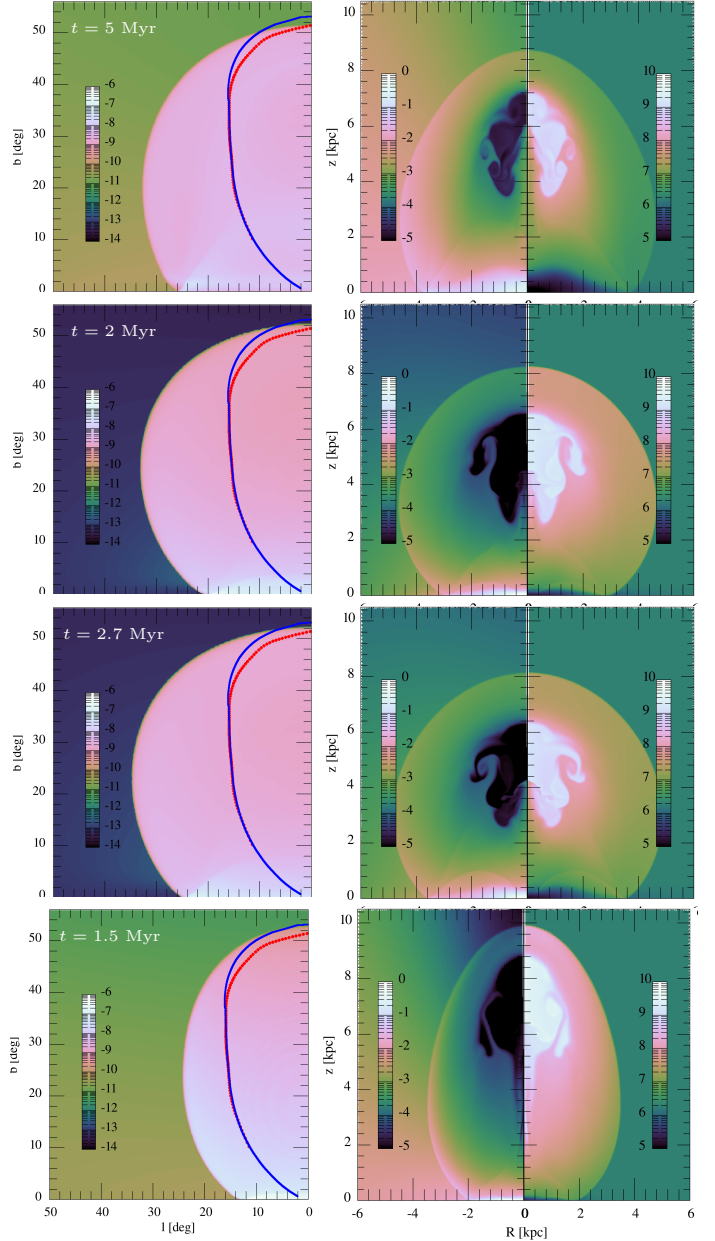


Figure 4. Variations on IL injection: each row is similar to the bottom row of Figure 2, and uses the same notations, but with some parameter change: $f_h = 0.9$ (first row), $M_d = 1.2 \times 10^{11} M_\odot$ (second row), $M_b = 4 \times 10^{10} M_\odot$ (third row), and the three changes combined (bottom row). Simulation parameters (setups S2a–d, top to bottom) are provided in the right columns of Table 2.

(2020, hereafter ZG20), which focused on a specific Galactic model and so could not make the above general claim.

4 JETTED INJECTION

As concluded in §3, we are unable to reproduce the observed FB geometry using non-directed injection, for any plausible Galactic model. We are therefore reduced to considering jetted injection scenarios, where a new dimensional scale

is introduced into the problem by means of the conserved momentum $p_z = p_j$ deposited in the axial, z direction, or interchangeably by the initial radial velocity v_j introduced in the small, $0 < \theta < \theta_j$ opening cone.

With such jetted injection models, we find that the observed FB geometry can be nicely reproduced in two distinct ways. A sufficiently energetic, slow initial jet can reproduce acceptable edges for simulated FBs that are presently still in their ballistic stage, whereas the converse — an initially fast, low-energy jet — can reproduce acceptable edges of non-ballistic FBs already in their slowdown phase.

At early times, the injected flow evolves ballistically in both cases, with the head of the bubble (subscript H) moving at a near constant velocity $v_H(t) \equiv \dot{z}_H \simeq v_j$. After the flow accumulates a mass M larger than the initial deposited mass M_j , the flow inevitably starts slowing down, with $v_H(t) \sim t^{-\tau_v}$ typically following a power-law decay with index $\tau_v > 0$. It is not yet known if the FBs observed today are in the former, ballistic stage or in the latter, slowdown stage, so we examine both scenarios. One can further split the ballistic forward evolution of a jetted bubble into two stages according to the sideways expansion being either ballistic or non-ballistic (Irwin et al. 2019), but we avoid this distinction here.

The mass M swept up by the bubbles is strongly dominated, for plausible Galactic models, by the halo, CGM component, exceeding the swept-up disc mass by about two orders of magnitude. For a $\rho_h \propto r^{-\alpha}$ CGM distribution, the present-day FBs are thus in the ballistic stage if the injected mass M_j satisfies

$$\frac{M_j}{2} \equiv \frac{E_j}{v_j^2} \gtrsim \frac{M}{2} \simeq \pi \theta_j^2 \int r^2 \rho_h(r) dr \simeq \frac{\pi \theta_j^2 \rho_h(z_H) z_H^3}{3 - \alpha}, \quad (11)$$

where $z_H \simeq 10$ kpc is the present-day height of the bubbles, and we approximated θ_j as small; recall that E and M pertain to the sum of both hemispheres. Conversely, the FBs have already transitioned into the slowdown phase if $M_j \lesssim M$, which may be written for $\alpha = 3/2$ as

$$\frac{E_j}{3 \times 10^{55} \text{ erg}} \lesssim \left(\frac{\theta_5 \beta_j}{0.01} \right)^2 z_{10}^3 \rho_4 \simeq (10^3 \beta_{\perp})^2 z_{10}^3 \rho_4, \quad (12)$$

where we defined $z_{10} \equiv z_H/10$ kpc, $\theta_5 \equiv \theta/5^\circ$, $\rho_4 \equiv \rho_h(z_H)/4 \times 10^{-4} m_p \text{ cm}^{-3}$, and the sideways initial velocity $\beta_{\perp} \equiv \beta_j \theta_j$. One can equivalently replace v_j by the conserved $2E_j/p_j$.

After developing in §4.1 a simple analytic model for the jetted bubbles in both regimes, we simulate the two scenarios in §4.2. We examine different variants of such bubbles, as described for jetted injection in §2.2, and compare the bubbles as they reach $b \simeq 52^\circ$ with the model and with the observed FBs.

4.1 Stratified model for jetted bubbles

Before discussing the simulated bubbles, it is useful to derive some relevant scaling relations using a simple toy model. Sufficiently far above the Galactic disc, the mass accumulated by the bubble is dominated by halo material, which has an approximately one-dimensional distribution around a narrow jet. The ambient medium can therefore be approximated as an isothermal, $\rho \propto z^{-\alpha}$, planar atmosphere, where

in our simulations $\alpha \simeq 1.5$. The fairly narrow FBs, when interpreted as arising from thin initial jets, are thus amenable to a simplified model that approximates the flow behind the head of the bubble as quasi two-dimensional, propagating perpendicular to the z axis.

Such a piecewise planar, or stratified, model is sufficient for capturing the main properties of the simulated flow, as we show for the ballistic bubbles in §4.1.1, and for bubbles in their slowdown phase in §4.1.2. More sophisticated modeling, for example using the Kompaneets approximation (Irwin et al. 2019, and references therein, for a simplified ambient model and $\gamma = 4/3$) is less useful here, because we find that (i) the ballistic phase plays an important role in the FBs; (ii) even in the slowdown phase, the injected momentum plays a key role; and (iii) post-shock pressure variations across the bubble surface are not small for slowing-down FBs.

We find that the structure and velocity of the jet are modified in the initial, injection stage, especially in the high v_j regime used to produce bubbles reaching the slowdown phase. We therefore use subscript k instead on j to refer to the actual jet parameters immediately after its $0 < t < t_j$ launching.

4.1.1 Ballistic regime

Consider our simple jetted setup deep in the ballistic regime. Here, the bubble has a height

$$z_H(t) \simeq v_k t, \quad (13)$$

so an observed FB with $z_H \simeq 10$ kpc would be of age

$$\mathbb{T} \simeq z_H/v_k \simeq 3.3 z_{10} \beta_{-2}^{-1} \text{ Myr}. \quad (14)$$

where $\beta_{-2} \equiv \beta_k/0.01$. At its top, the bubble head has a width

$$R \simeq \theta_k z_H \simeq 0.9 z_{10} \theta_5 \text{ kpc}, \quad (15)$$

where the forward shock is strong, of Mach number

$$\Upsilon \simeq \frac{v_k}{c_s} \simeq 14 \beta_{-2} \left(\frac{T_h}{2 \times 10^6 \text{ K}} \right)^{-1/2}. \quad (16)$$

Here, we defined $\theta_5 \equiv \theta_k/5^\circ$. At lower, $z < z_H$ heights, the bubble initially has a half-width

$$R(z, t = z/v_k) \simeq \theta_k z, \quad (17)$$

but later necessarily expands due to the pressure of the shocked CGM.

Let us parameterise the geometry of the bubble as $R_b(z, t) \simeq z \Theta(z, t)$, in the small angle, $\Theta \ll 1$ limit. A crude way to estimate the shape $R_b(z, t = \mathbb{T})$ of the evolved ballistic bubble is to consider each fixed- z slice as a separate layer, independently expanding sideways, *i.e.*, in the R direction. The pressure transferred to this slice as it is first shocked by the head of the bubble is, according to the shock jump conditions, $P(z) \simeq (3/4) \rho_h(z) v_H(z)^2$. For simplicity, we approximate the subsequent slice evolution as sideways expansion with a characteristic velocity $v_R(z, t) = f_R \dot{R}_b$, where f_R is a dimensionless factor of order unity, chosen as $f_R \simeq 1/2$ in light of the nearly linear velocity profile anticipated behind a cylindrical strong shock. We roughly equate the associated kinetic energy per unit

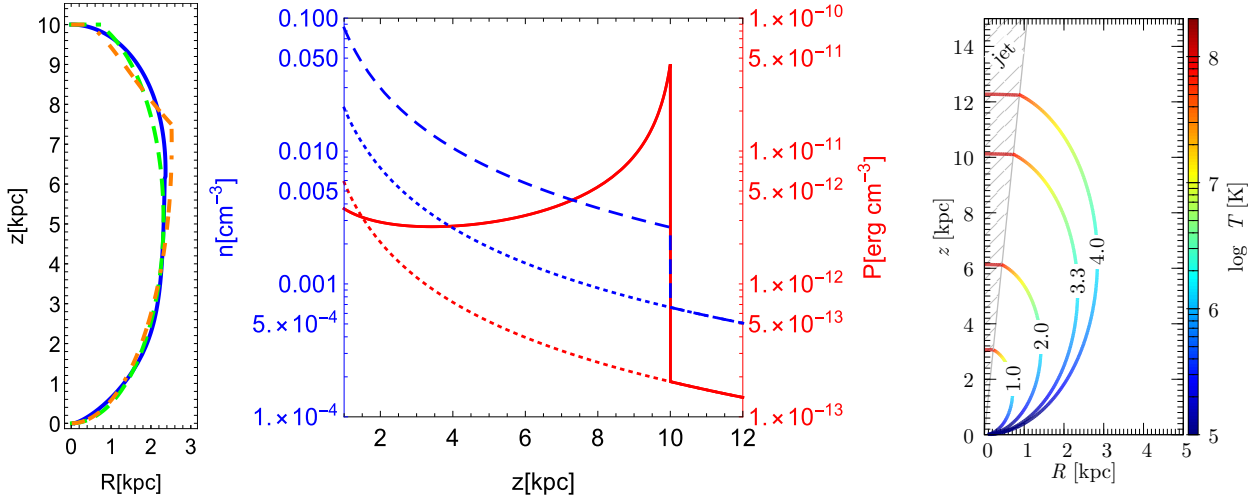


Figure 5. Left panel: ballistic (with $\theta_k = 4^\circ$; dashed green) and slowdown (with $\theta_k = 2^\circ.5$, $z_s = 7.5$ kpc and $f_q = 1/4$; dot-dashed orange) models for the bubble edge at $z_H = 10$ kpc, compared with a phenomenological geometry previously used to reproduce the projected observations (Keshet & Gurwich 2018, solid blue). Middle panel: density (dashed blue; left axis) and pressure (solid red; right axis) profiles of the ballistic model with a $\rho_h = 4 \times 10^{-4} m_p (r/10 \text{ kpc})^{-1.5}$ CGM and $\beta_k = 0.01$. The profiles before launching the jet are also shown (dotted); subsequent evolution including the reverse shock and contact discontinuity are not. Right panel: ballistic evolution of the shock front according to Eq. (19) at different times as noted on the curves (in Myr). The color in each curve shows the shock temperature from Eq. (26) except within the jet cone where the temperature is given from Eq. (24).

height with the thermal energy initially deposited by the head, $4\rho_h(z)\pi R_b^2(z,t)v_R^2(z,t)/2 \simeq \pi(z\theta_k)^2(3/2)P(z)$.

Solving the resulting ODE,

$$2z\Theta\dot{\Theta} = 3v_H(z)\theta_k, \quad (18)$$

with the ballistic behavior $v_H(z) \simeq v_k$ and the initial condition (17), we then obtain

$$\Theta(z,t)^2 \simeq 3\left(\frac{v_k t}{z} - 1\right)\theta_k + \theta_k^2, \quad (19)$$

in good agreement with the FB shape inferred from observations. For small θ_k , and for z not too close to z_H , we may approximate the bubble shape by

$$R_b(z,t)^2 \simeq 3[z_H(t) - z]\theta_k z. \quad (20)$$

Note that for a fixed $z \gg R$, at late times $R(z) \sim t^{1/2}$ agrees with the expected self-similar cylindrical expansion.

For small θ_k , the maximal half-width

$$R_{\max}(t) \simeq \frac{v_k t}{2} \sqrt{3\theta_k}, \quad (21)$$

is obtained at the bubble half-height, $z \simeq z_H/2$. Hence, for the evolved bubble

$$R_{\max}(t = \mathbb{T}) \simeq \frac{z_H}{2} \sqrt{3\theta_k} \simeq 2.6\theta_5^{1/2} z_{10} \text{ kpc}. \quad (22)$$

Equation (21) also implies that the latitudinal and longitudinal widths of the bubble at any given time are

$$\begin{aligned} \Delta b &\simeq \frac{z_H}{R_\odot} \simeq 20.1^\circ \beta_{-2} t_{\text{Myr}}; \\ \Delta l &\sim \frac{R_{\max}(t)}{R_\odot} \simeq 5.3^\circ \beta_{-2} t_{\text{Myr}} \theta_5^{1/2}. \end{aligned} \quad (23)$$

Non-ballistic corrections, becoming gradually larger as the swept up mass M approaches the injected mass M_j near the slowdown phase, can render the bubbles somewhat older and wider than estimated here. The geometry of the bubble edge for $z_H = 10$ kpc is demonstrated in Figure 5 (left

panel). This one-zone approximation for the sideways expansion leaves out substructure associated with the contact discontinuity and the reverse shock.

The shock is fastest at the top of the bubble, where the downstream temperature is

$$T_i \simeq \frac{3\mu_m m_p}{16k_B} v_k^2 \simeq 1.2 \times 10^8 \beta_{-2}^2 \text{ K}. \quad (24)$$

Note that the electron temperature may be considerably lower than the ion temperature close to the shock, as the ion–electron equilibration time-scale can be shorter than the dynamical time-scale (z_H/\mathbb{T}) of the shock (e.g., KG18). The sideways velocity $v_R = f_R z \dot{\Theta}$ of the shock at a given z and t is given by

$$v_R \simeq \frac{3v_k \theta_k}{4\Theta(z)} \simeq \frac{3}{4} v_k \left/ \sqrt{1 + \frac{3}{\theta_k} \left[\frac{z_H(t)}{z} - 1 \right]} \right., \quad (25)$$

indicating that the temperature behind a strong sideways shock,

$$T_R \simeq \frac{3}{16} \frac{\mu_m m_p}{k_B} \left(\frac{3v_k \theta_k}{4\Theta} \right)^2, \quad (26)$$

is constant at a given Θ , but gradually declines in time at a fixed z . The evolution of the shape and temperature is shown in the right panel of Fig 5. Note that, the above temperature is only derived from the sideways expansion and is expected to fail near $\Theta \sim \theta_k$ since the shock velocity in this region will be dominated by vertical motion of the jet.

Figure 5 (middle panel) illustrates the vertical profiles $n(z) \simeq 4(\mu_m m_p)^{-1} \rho_h(z) \theta_k^2 / \Theta(z)^2$ of particle number density and $P(z) \simeq (3/4) \rho_h(z) v_k^2 \theta_k^2 / \Theta(z)^2$ of pressure, for the one-zone model, assuming a homogeneous isothermal expansion near the axial.

The above arguments suggest that the FBs may indicate a ballistic flow arising from an abrupt injection of energy and momentum, provided that the ratio $E_j/v_j^2 \propto p_j^2/E_j$ is

sufficiently high to satisfy (11), that the opening angle of the jet is of order 4° , and that the FB age is given by (14). This possibility is studied numerically in §4.2.1.

4.1.2 Slowdown regime

Next, consider the same jetted setup, but now deep in the slowdown regime. Here, the nearly planar shock of area $\sim \pi\theta_k^2 z_H^2$ (the exact value is immaterial for the present argument) at the head of the jet propagates at an increasingly slower velocity $v_H(t) \propto t^{-\tau_v}$ into the approximately $\rho_h \propto z^{-\alpha}$ CGM.

We approximate the momentum of the shocked mass, $p_z \simeq f_p \pi \theta_k^2 \rho_h(z_H) z_H^3 v_M / (3 - \alpha)$, as some fraction f_p of the product of the swept-up mass M and the velocity $v_M \simeq (3/4)v_H$ inferred from the shock jump conditions just behind the shock, where all velocities are measured in the Galactic frame. Fresh mass accreted through the shock raises the momentum of the bubble at a rate $\dot{p}_z^+ = \pi(\theta_k z_H)^2 \rho_h(z_H) v_H v_M$, so momentum conservation implies that $dp_z/dt + \dot{p}_z^+ = 0$.

The resulting ODE,

$$\frac{\partial \ln[\rho_h(z_H) z_H^3 v_H]}{\partial \ln z_H} = -f_q^{-1}, \quad (27)$$

where $f_q \equiv f_p/(3 - \alpha)$, leads to $v_H \propto z_H^{-(f_q^{-1} + 3 - \alpha)}$, and hence to the late-time power-law indices

$$0 < \tau_z \equiv \frac{d \ln z_H}{d \ln t} \simeq \frac{f_q}{1 + (4 - \alpha)f_q}, \quad (28)$$

and

$$0 < \tau_v \equiv -\frac{d \ln v_H}{d \ln t} = 1 - \tau_z = \frac{1 + (3 - \alpha)f_q}{1 + (4 - \alpha)f_q}. \quad (29)$$

For $\alpha = 3/2$, typical estimates $1/5 \lesssim f_q \lesssim 1/3$ yield a small $2/15 \lesssim \tau_z \lesssim 2/11$ and a near-unity $9/11 \lesssim \tau_v \lesssim 13/15$, consistent with the simulations shown below.

More precisely, twice integrating Eq. (27) yields

$$z_H(t > t_s) \simeq \left[1 + \left(\frac{t}{t_s} - 1 \right) \tau_z^{-1} \right]^{\tau_z} z_s, \quad (30)$$

where z_s and t_s are the height and time of the transition from ballistic to slowdown phases, derived toward the end of this subsection. The implied age of the bubble,

$$\mathbb{T} \simeq \left[\tau_v + \left(\frac{z_H}{z_s} \right)^{1/\tau_z} \tau_z \right] t_s, \quad (31)$$

is the sum of a linear, $t_s \propto z_s$ ballistic period and a non-linear, $\propto (z_H/z_s)^{1/\tau_z}$ slowdown period. As τ_z is a small number, a low transition height z_s would imply that \mathbb{T} is dominated by the slowdown phase. A given bubble age thus imposes a lower limit on z_s ,

$$\frac{z_s}{z_H} > \left(\frac{z_H \tau_z}{c \beta_k \mathbb{T}} \right)^{\tau_z/\tau_v} > \left(\frac{z_H \tau_z}{c \mathbb{T}} \right)^{\tau_z/\tau_v}, \quad (32)$$

and slowdown at $z_s < z_H$ would require $\beta_k \mathbb{T} > z_H/c$, as illustrated in Figure 6. For example, for a $z_H = 10$ kpc, $\mathbb{T} = 3$ Myr bubble and $f_q = 1/4$, the FBs can be in the slowdown phase only if $z_s \gtrsim 3.1 \beta_k^{-2/11}$ kpc > 3.1 kpc (blue arrow in the figure); requiring slowdown implies that the average normalized velocity till t_s is $\beta_k > z_H/c\mathbb{T} \simeq 0.01$.

To estimate the shape of the bubble in the slowdown

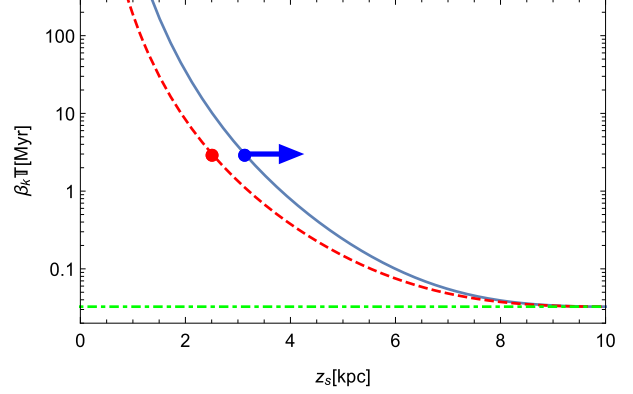


Figure 6. Bubble age \mathbb{T} as a function of the height z_s of the transition from ballistic to slowdown phases, weighted by the normalized velocity $\beta_k \equiv z_s/ct_s < 1$ of the jet before the transition, shown for $f_q = 1/4$ (solid blue) and $f_q = 1/3$ (dashed red) with a bubble height $z_H = 10$ kpc. A given bubble age thus imposes lower limits on z_s (discs and arrow) and on β_k (dot-dashed), as illustrated for $\mathbb{T} = 3$ Myr.

regime, assume for simplicity that the sideways expansion remains ballistic for some duration after t_s . We solve the same sideways expansion ODE (18) as in the ballistic case, but now incorporating the slowing down vertical velocity

$$v_H(z > z_s) \simeq (z/z_s)^{-(f_q^{-1} + 3 - \alpha)} v_k, \quad (33)$$

which corresponds to a Mach number

$$\Upsilon \simeq \frac{v_k}{c_s} \simeq 14 (z/z_s)^{-(f_q^{-1} + 3 - \alpha)} \beta_{-2} \left(\frac{T_h}{2 \times 10^6 \text{ K}} \right)^{-1/2} \quad (34)$$

at the top of the bubble. The initial sideways-expansion condition (17) of the ballistic regime now pertains only to $t < t_s$, and is supplemented by the slowdown-phase condition

$$R_b[z = z_H(t > t_s), t > t_s] \simeq \theta_k z. \quad (35)$$

For $z < z_s$, the bubble geometry is still formally given by (19), whereas above the transition height the bubble narrows sharply with increasing z ,

$$\Theta(z > z_s, t)^2 \simeq 3 \left\{ \left[\frac{z_H(t)}{z} \right]^{1/\tau_z} - 1 \right\} \tau_z \theta_k + \theta_k^2. \quad (36)$$

The combined solution (19) and (36) is illustrated in Figure 5 for $f_q = 1/4$. For small θ_k and for z not too close to z_H , we may approximate

$$R_b(z > z_s, t)^2 \simeq 3 \theta_k \tau_z z_H^{1/\tau_z} z^{-\tau_v/\tau_z}. \quad (37)$$

Anticipating the widest part of the bubble at $z \simeq z_s$, Eq. (19) indicates that

$$R_{\text{max}}(t) \simeq (3 \theta_k v_k z_s t)^{1/2} \simeq 2.0 \left(\beta_{-2} \theta_5 t_1 \frac{z_s}{5 \text{ kpc}} \right)^{1/2} \text{ kpc} \quad (38)$$

in the $t \equiv t_1$ Myr $\gg t_s$ regime. As the bubble necessarily narrows from z_s to z_H , the observed shape of the FBs indicates that $z_s \gtrsim z_H/2$.

In addition to the stratified flow approximation, the above solution to the shape of the bubble in the slowdown phase is also based on the simplifying assumptions of a sudden transition from ballistic to slowdown behaviors, and a fixed head opening-angle $\Theta[z_H(t), t] = \theta_k$ at all times. In

practice, the transition is smooth, and the tip of the head may gradually expand. Consequently, while the non-ballistic profile in [Figure 5](#) provides a reasonable approximation to the simulated slowing-down bubbles, the sharp break at z_s is smoothed out in our simulations. Therefore, instead of estimating the maximal width of the evolved bubble at $z = z_s$,

$$R_{\max}(t = \mathbb{T}) \simeq (3\tau_z\theta_k)^{1/2} \left(\frac{z_H}{z_s}\right)^{1/2\tau_z} z_s, \quad (39)$$

we may for simplicity use $z \simeq z_H/2$, such that

$$R_{\max}(t = \mathbb{T}) \simeq \left(\frac{3}{2}\theta_k v_k z_H \mathbb{T}\right)^{1/2}. \quad (40)$$

As $v_k \mathbb{T} > z_H$ in the slowdown regime, nominal parameters yield $\theta_k \lesssim 2^\circ$.

A jet generating FBs in the slowdown regime is faster and lower in energy and in mass than its ballistic counterpart, and thus more sensitive to the numerical setup. Assuming that the setup loads the jet with an additional, spurious mass M_0 and slows it down to a velocity $v_k < v_j$, we equate the total injected mass with an uncertainty factor f_m times the swept-up mass to estimate the slowdown at time $t_s \equiv z_s/v_k$ and height

$$z_s \simeq \left(\frac{M_0 + 2E_j/v_j^2}{2\pi\theta_k^2 C_\rho f_m}\right)^{\frac{1}{3-\alpha}} \simeq 10 \frac{(E_{55}/4f_q C_4)^{2/3}}{(\beta_{-2}\theta_5)^{4/3}} \text{ kpc}, \quad (41)$$

where $C_\rho \equiv z^\alpha \rho_h(z) \equiv C_4(10 \text{ kpc})^\alpha \rho(z = 10 \text{ kpc})/(4 \times 10^{-4} m_p \text{ cm}^{-3})$ is a constant, and $E_{55} \equiv E_j/10^{55} \text{ erg}$. The last expression in [Eq. \(41\)](#) pertains to $\alpha = 3/2$, approximates $f_m \simeq f_q$, and assumes a negligible M_0 . Equation (41) is more accurate than the conditions (11) and (12) for determining the phase of the bubble.

4.1.3 Ballistic or slowing-down FBs?

In spite of the lowered dimensionality of the stratified toy models outlined in [§4.1.1](#) and [§4.1.2](#), in which each layer of constant z evolves independently, these models capture much of the bubble structure and scaling we find in the simulations described below in [§4.2.1](#) and [§4.2.2](#), respectively.

In the case of FBs in the slowdown phase, the numerical launching of the faster, less energetic jet is more delicate, and the outcome is more sensitive to details. For simplicity, above we neglected the finite, $t_j \simeq 0.4 \text{ Myr}$ injection stage of the jet, during which interactions with ambient gas over a substantial, $z_j \lesssim t_j v_j \simeq 1.2 (t_j/0.04 \text{ Myr})(\beta_j/0.1) \text{ kpc}$ height can modify the jet parameters. In particular, for a sufficiently high v_j , the mass M_0 accumulated during this stage can exceed the injected mass M_j , the jet can be slowed down by a factor v_k/v_j of a few, and it can become broadened or pinched by a noticeable factor θ_k/θ_j .

For a fast injected jet, the strong initial shear may disrupt the jet, reshape it, focus it, or broaden it via partial thermalisation of the jet-base through viscosity or KHL. Consider in particular the viscous radial acceleration of gas around the jet, boosting the initial $v_R = 0$ to $v_R(t) \simeq (t v_j \mu)/(\rho \Delta R \Delta z)$, where $\Delta R \simeq (t \mu/\rho)^{1/2}$ is the width of the shear layer and Δz is the typical scale for flow variations in the z direction. Then the effective opening angle becomes

$$\theta_{\text{eff}} \simeq v_R(t)/v_j \simeq (t \mu/\rho)^{1/2} / \Delta z \propto \mu^{1/2}, \quad (42)$$

with some dependence on t_j arising from t and possibly also from ρ and Δz , depending on details.

We conclude that the FBs are either presently in the ballistic stage, or were at the ballistic stage as recently as when the bubbles were at a height $z_s \gtrsim 5 \text{ kpc}$, based on four different observations: (i) the bubbles are not very old, so [Eq. \(32\)](#) constrains z_s ; (ii) the Mach number is high, so [Eq. \(34\)](#) similarly constrains z_s ; (iii) the bubbles are fairly cylindrical, as discussed below [Eq. \(38\)](#); and (iv) the initial opening angle cannot be too small, so z_s is constrained by [Eq. \(39\)](#),

$$\frac{z_s}{z_H} \simeq \left(\frac{R_{\max}/z_H}{\sqrt{3}\theta_k \tau_z}\right)^{\frac{2\tau_z}{2\tau_z-1}} \simeq 0.9 \left(\frac{4R_{\max}}{z_H}\right)^{-\frac{4}{9}} \theta_5^{2/9}, \quad (43)$$

where the last estimate pertains to $f_q = 1/4$. Due to this weak dependence upon θ_k , a small, say $z_s < 1 \text{ kpc}$ would require an early jet opening angle smaller than an arcsecond. Adopting $z_s \gtrsim 5 \text{ kpc}$, [Eq. \(41\)](#) implies that

$$\frac{E_{55}}{(\beta_{-2}\theta_5)^2} \gtrsim 0.4(4f_q)C_4. \quad (44)$$

In both ballistic and slowdown scenarios, a high Mach number Υ at the top of the bubble requires $\beta_{-2} \gtrsim 0.4\Upsilon_5$, where $\Upsilon_5 \equiv \Upsilon/5$, and the thickness of the bubbles requires $\theta_k \lesssim 4^\circ$. These results become approximate equalities in the ballistic case, whereas an extended slow-down phase requires a much faster and narrower jetted injection. The FBs are in the ballistic stage if they are energetic or slow, $E_{55} \gtrsim 3(\beta_{-2}\theta_5)^2$, in which case $E_{55} \gtrsim 2\beta_{-2}^2 \gtrsim 0.2\Upsilon_5^2$ and $\mathbb{T} \simeq 3.3\beta_{-2}^{-1} \text{ Myr} \lesssim 8\Upsilon_5^{-1} \text{ Myr}$. The FBs are in the slowdown phase if $E_{55} \lesssim 3(\beta_{-2}\theta_5)^2$, in which case $0.05\Upsilon_5^2\theta_5^2 \lesssim E_{55} \lesssim 2\beta_{-2}^2$ and $\mathbb{T} \simeq 1.4(\beta_{-2}\theta_5)^{-1} \text{ Myr} \lesssim 4(\Upsilon_5\theta_5)^{-1} \text{ Myr}$. Such slowing-down FBs can still be energetic, provided that β_{-2} is large, but their age would then be of order a Myr only if θ_5 is small.

4.2 Jetted simulations

We carry out a suite of simulations that generate *Fermi*-like bubbles in both ballistic and slowdown phases. The parameters and resulting bubble properties for a sample of such simulations are listed in [Table 3](#). [Figure 7](#) shows our nominal ballistic (setup J1; top row) and slowdown (J2; bottom panel) simulated bubbles. Unlike non-directed injection, jetted injection gives rise to forward shocks that do agree well with the observed FB edges, as inferred from the stratified models of [§4.1](#) and confirmed by our simulations. As the figure demonstrates, this agreement holds in both ballistic and slowdown regimes, albeit with different parameters, as seen in the table.

The figure indicates that the inner structure of the ballistic and slowing-down bubbles differ substantially, the former showing an inner cylindrical shock surrounded at its top by an irregular contact discontinuity surface, and the latter showing a bubble-like contact discontinuity trailing the shock. The two types of bubbles differ qualitatively also in their evolution and parametric dependence, as outlined in [§4.1](#) and explored numerically below.

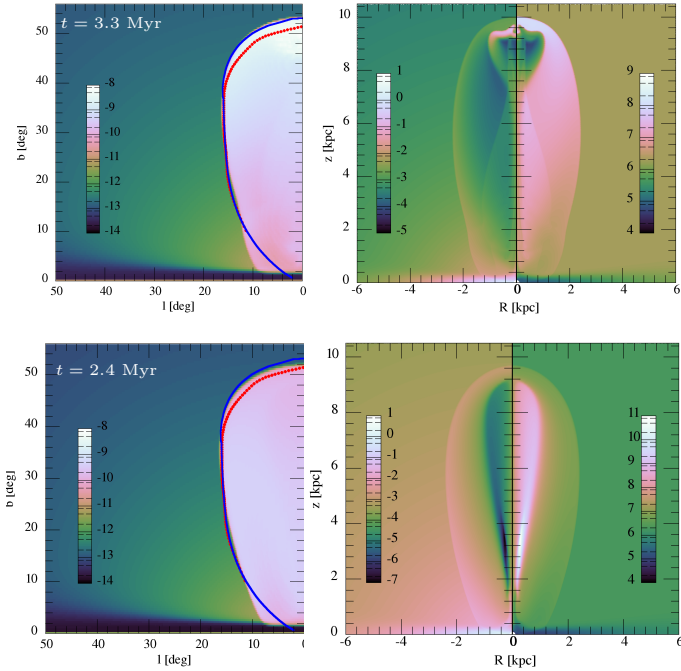


Figure 7. Simulated FBs generated by jetted injection, in their ballistic (top; setup J1) and slowdown (bottom; setup J2) phases. The simulation parameters are provided in Table 3. Notations are the same as in Figure 2. The slowdown bubble is somewhat younger as its ballistic stage was very short due to the much faster injection.

4.2.1 Ballistic bubbles

In our fiducial ballistic simulation, denoted J1, an energy 3×10^{56} erg is injected with $\beta_j = 0.01$ inside an opening angle $\theta_j = 5^\circ$ for a duration $t_j = 0.04$ Myr, resulting in a *Fermi*-like bubble reaching the designated latitude at $\mathbb{T} \simeq 3.3$ Myr, as depicted in Figure 7 (top row). The contact discontinuity (seen towards the top of the bubble) and inner shock are also evident in the pressure and entropy distributions presented in Figure 8 (left panel). These distributions indicate a non-homogeneous inner structure, with a very low pressure region behind the bubble head. However, the pressure just behind the shock and throughout the bubble is fairly uniform, varying by only a factor of a few throughout the surface of the bubble.

The low pressure region can be identified as the unperturbed jet material that has been pinched by the high pressure region behind the ballistically expanding shock. In a simple picture, this region should be conical in shape, with a head half-width $R_{lp} \simeq z_H \theta_j$ and a length $\Delta z_{lp} \simeq v_j R_{lp} / c_s$ given by the R_{lp} sound crossing time, where $c_s \simeq (3\gamma/16)^{1/2} v_j$ is the sound speed behind the shock. For $v_j = 0.01 c$ and $\theta_j = 5^\circ$, $\Delta z_{lp} \simeq 1.5$ kpc is consistent with the simulated region in Figure 7.

The figure also shows the temporal evolution of the bubble, in space (middle panel) and in projection (right). After the initial ~ 0.6 Myr, the height and maximal half-width of the bubble are well fit (green curves) by $z_H \sim 3.33 t_1^{0.928 \pm 0.004}$ kpc and $R_{\max} \sim 0.79 t_1^{0.92 \pm 0.02}$ kpc, where $t_1 \equiv t/\text{Myr}$. This evolution is consistent with the expected

linear behavior (13) and (21), with $v_k \simeq v_j$ and $\theta_k \simeq \theta_j$ almost unaffected by the initial transients, and with only a $\sim 8\%$ slowdown during $0 < t < \mathbb{T}$. The projected coordinates are well fit at this stage by $b \simeq 22^\circ .2 t_1^{0.75 \pm 0.02}$ and $\Delta l \sim 5^\circ t_1^{0.99 \pm 0.02}$, in agreement with the model (see Eq 23).

The ballistic bubbles and their internal structures are not much affected by viscosity, as the associated jet velocities ($\beta_j \sim 0.01$) are relatively low. We have confirmed this behavior with several viscous simulations, of Spitzer viscosity capped at $\mu_{\max} = 10 \text{ g cm}^{-1} \text{ s}^{-1}$ (as discussed in sec 2) and even with an excessive, fixed $\mu = 40 \text{ g cm}^{-1} \text{ s}^{-1}$ throughout the simulation box.

We carry out a suite of simulations that generate *Fermi*-like bubbles in their ballistic stage. A representative sample of such simulations, including our fiducial setup J1 and its variants J1a through J1d, are summarised in the middle columns of Table 3, and are presented in Figure 9 at the times (displayed in the upper left corner of each row) when each bubble reaches the designated latitude. The table provides the central measured properties of each simulated bubble: its age \mathbb{T} and maximal half-width Δl .

By separately varying each of the setup parameters, one at a time, we derive the functional dependencies of the bubble age

$$\mathbb{T} \simeq 3.2 \left(\frac{E_j}{3 \times 10^{56} \text{ erg}} \right)^{-0.030 \pm 0.004} \beta_{-2}^{-0.96 \pm 0.01} \theta_5^{-0.003 \pm 0.031} \times t_{0.04}^{0.007 \pm 0.004} \text{ Myr}, \quad (45)$$

its maximal half-width

$$R_{\max} \simeq 2.2 \left(\frac{E_j}{3 \times 10^{56} \text{ erg}} \right)^{-0.032 \pm 0.005} \beta_{-2}^{-0.11 \pm 0.02} \theta_5^{0.40 \pm 0.03} \times t_{0.04}^{-0.017 \pm 0.002} \text{ kpc}, \quad (46)$$

and maximal longitude

$$\Delta l \simeq 16^\circ .3 \left(\frac{E_j}{3 \times 10^{56} \text{ erg}} \right)^{-0.024 \pm 0.004} \beta_{-2}^{-0.07 \pm 0.02} \theta_5^{0.41 \pm 0.03} \times t_{0.04}^{-0.014 \pm 0.005}, \quad (47)$$

valid in the close vicinity of the fiducial J1 setup. Such individual parametric scans are illustrated in Figure 10. Here, we defined $t_{0.04} \equiv t_j/0.04$ Myr. The fits (45) and (46) are in good agreement with the model Eqs. (14) and (22), showing that the anticipated age $\mathbb{T} \propto \beta_j^{-1}$ and half-width $R_{\max} \propto \theta_j^{1/2}$ of the ballistic bubble are nearly independent of other parameters.

As expected, these scaling relations break down when the setup parameters are modified substantially away from the J1 setup. In particular, if (only) the energy is lowered considerably, non-ballistic corrections emerge, and we obtain

$$\mathbb{T} \sim [3.1 + (E_j/2.1 \times 10^{55} \text{ erg})^{-0.80 \pm 0.03}] \text{ Myr} \quad (48)$$

and

$$\Delta l \sim [13^\circ .8 + 1^\circ .0 (E_j/3.0 \times 10^{56} \text{ erg})^{-0.39 \pm 0.01}], \quad (49)$$

as shown in Figure 10. These results indicate that $\lesssim 7\%$ non-ballistic corrections are present in the J1 bubble.

The properties of the simulated ballistic bubbles are approximately independent of the injection parameters t_j and r_0 (in the nominal ranges $0.25 < t_{0.04} < 2$ and

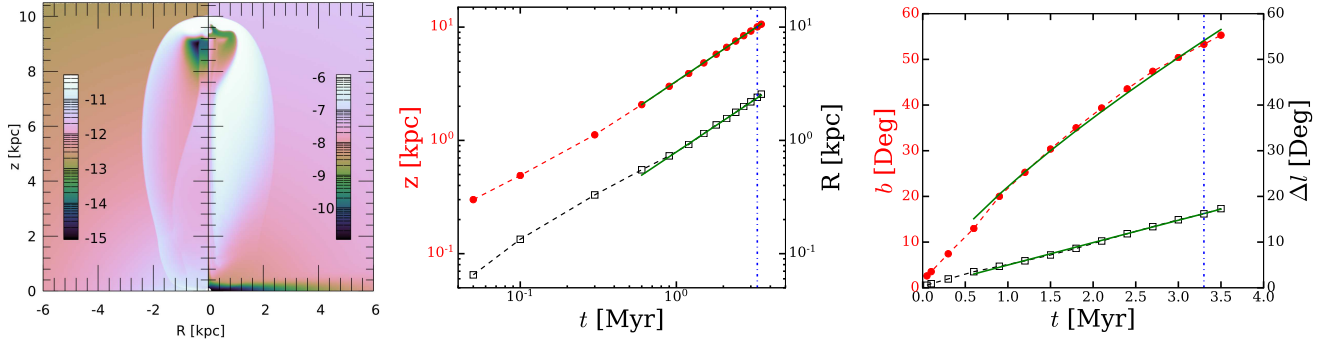


Figure 8. Thermal structure (left panel) and spatial (middle) and projected (right) evolution of our fiducial ballistic bubble (setup J1). Left panel: logarithmic pressure (in erg cm^{-3} ; left half of left panel) and entropy (shown as the adiabat $Pn^{-\gamma}$ in erg cm^2 units; right half) distributions highlight the inner shock and contact discontinuity. Middle and right panels: the temporal evolution of the height (red discs with left axis) and half-width (black squares; right axis) of the bubble is shown, along with power-law fits (solid green for $t > 0.6$ Myr; see text) and the cutoff time (dot-dashed blue) at the designated latitude.

Table 3. Parameters varied in the select jetted injection simulations presented in Figure 7 (top panel) and Figure 9. Many additional simulations (not shown) with varying parameters are used to approximate parameter dependencies, as illustrated in Figures 10 and 13.

Parameter	Definition	Ballistic bubbles					Slowing-down bubbles				
		J1	J1a	J1b	J1c	J1d	J2	J2a	J2b	J2c	J2d
M_d [$10^{10} M_\odot$]	Disc mass			6.0			6.0	6.0	6.0	6.0	12.0
M_b [$10^{10} M_\odot$]	Bulge mass			2.0					2.0		
f_h	CGM rotation			0					0		
E_j [10^{56} erg]	Injected energy	3.0	2.0	3.0	3.0	3.0	0.25	0.3	0.3	0.3	0.25
$\beta_j = v_j/c$	Injected velocity	0.01	0.01	0.015	0.01	0.01	0.1	0.1	0.12	0.1	0.1
t_j [Myr]	Injection duration	0.04	0.04	0.04	0.04	0.01	0.04	0.04	0.04	0.06	0.04
θ_j	Injection opening angle	5°	5°	5°	3°	5°	4°	4°	4°	4°	4°
r_0 [kpc]	Inner boundary			0.1					0.1		
μ_{\max} [$\text{g s}^{-1} \text{cm}^{-1}$]	Viscosity (when included) limit	—	—	—	—	—	10	10	10	10	10
\mathbb{T} [Myr]	Bubble age (approximate)	3.3	3.3	2.2	3.3	3.2	2.4	1.5	2.5	2.0	1.0
Δl	Bubble half width (approximate)	16°	16°	16°	13°	16°	16°	12°	17°	15°	14°

$0.05 < r_0 < 0.25$). The results are also fairly independent of the Galactic model parameters. In particular, even extreme changes to the disc mass and halo rotation parameters have a rather negligible effect on the shape and age of the bubble.

4.2.2 Slowing-down bubbles

In our fiducial slowing-down FB simulation, denoted J2, an energy of 2.5×10^{55} erg is injected with velocity $\beta_j = 0.1$ inside an opening angle $\theta_j = 4^\circ$ for a duration of $t_j = 0.04$ Myr. This results in a *Fermi*-like bubble reaching the designated latitude at $\mathbb{T} \simeq 2.4$ Myr, as depicted in Figure 7 (bottom row). For such a lower energy, higher velocity jet, the amount of thermalisation near the jet-base is not numerically resolved, due to unresolved KHI. To deal with such artefacts, we introduce viscosity adopting Spitzer viscosity with a $\mu_{\max} = 10 \text{ g s}^{-1} \text{cm}^{-1}$ upper limit, as discussed in section 2.

The contact discontinuity trailing all parts of the slowing-down shock is evident in the figure, as well as in the corresponding pressure and entropy distributions presented in Figure 11 (left panel). Unlike in the ballistic bubble, this figure does not show any evidence of an inner shock or a low-pressure region trailing the bubble head, due to an earlier thermalisation of the low momentum ($2E_j/c\beta_j$) jet for a given energy, as explained in section 4. The pressure is

fairly uniform in the inner parts of the bubble, but pressure variations behind the shock span more than an order of magnitude across the surface of the bubble.

We find that in the fast injection domain, the initial jet emerging by the injection time t_j is substantially reshaped by the strong interactions with the ambient gas. Unlike the slow jets studied for ballistic bubbles, which are initially sustained as cones of opening angle $\theta_k \simeq \theta_j$, the present fast jets substantially narrow at their top, presenting as top-pinned bubbles. The upper structure of these initial jets are subsequently shaped by the interaction with the ambient gas, rather than by the initial jet parameters. Indeed, we find that the simulation results in the high velocity regime are not sensitive to the initial setup parameters $3^\circ \lesssim \theta_j \lesssim 5^\circ$ and $0.05 < r_0/\text{kpc} < 0.5$. Instead, a dependence on viscosity and injection time emerges, as anticipated in §4.1.3.

Figure 11 also shows (middle and right panels) the temporal evolution of the bubble. At early, $t \lesssim 0.5$ Myr times, the bubble grows approximately linearly both in height and in width, as expected in the ballistic phase. For the fast jets in this regime, the injection stage has a much stronger effect in slowing and reshaping the jet. From Eqs. (13) and (21), we estimate that $v_k \simeq 0.6v_j$ and $\theta_k \simeq 0.3$ (independent of θ_j). At late times ($t \gtrsim 0.5$ Myr), the bubble height grows noticeably slower, while its widening is only slightly diminished, as expected in the slowdown phase. The ballistic-to-slowdown

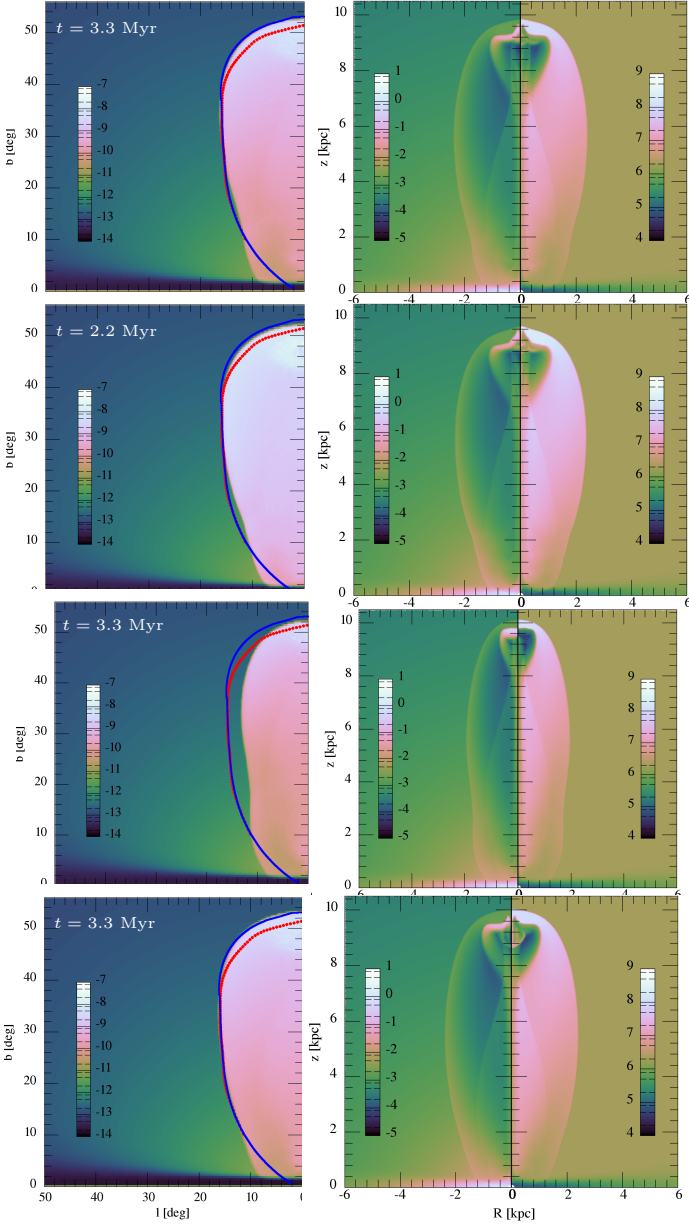


Figure 9. Select variations of the ballistic bubble setup, with parameters identical to J1 except $E_j = 2 \times 10^{56}$ erg (J1a; first row), $\beta_j = 0.015$ (J1b; second row), $\theta_j = 3^\circ$ (J1c; third row), and $t_j = 0.01$ Myr (J1d; fourth row). Notations are the same as in Figure 2.

transition can therefore be identified at $t_s \simeq 0.5$ Myr and $z_s \simeq 8$ kpc.

In the slowdown phase, the slow growth in height is well-fit by a power law, $z_H(t > 0.6 \text{ Myr}) \simeq 8.5t_1^{0.14}$ kpc, consistent with Eq. (28) provided that $f_q \simeq 1/5$. The widening of the bubble is not precisely a power law in this stage, slowing from $R_{\max}(t > 0.6 \text{ Myr}) \simeq 1.4t_1^{0.6}$ kpc to $R_{\max}(t > 1.8 \text{ Myr}) \simeq 1.5t_1^{0.5}$. The latter nicely matches (both in normalization and in power-law) the expected late-time behavior (38) for the above parameters. The projected dimensions of the bubble are best fit for $t > 0.6$ Myr by $b \simeq 46^\circ .3t_1^{0.13}$ and $\Delta l \sim 8^\circ .6t_1^{0.7}$.

We carry out a suite of simulations that generate *Fermi*-

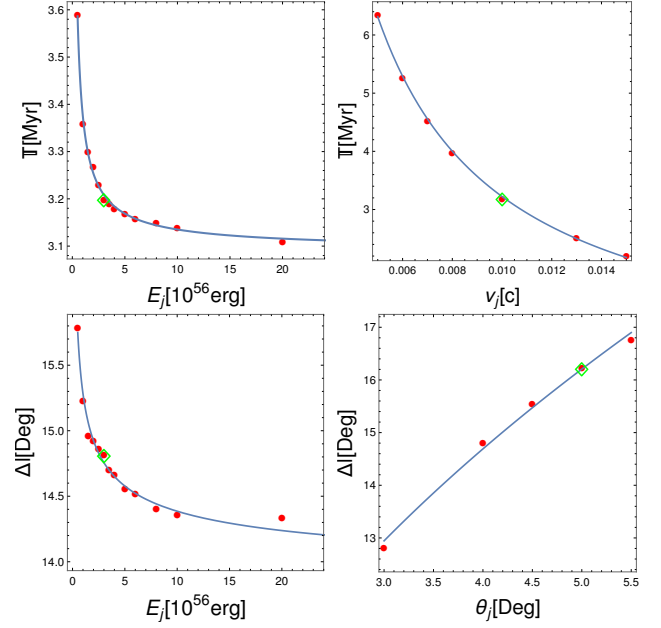


Figure 10. Best fit values (red discs) of \mathbb{T} (top row) and Δl (bottom) for setup J1 (green diamond) modified by single-parameter variations in E_j (left panels), v_j (top right) or θ_j (bottom right). Best fit profiles (see text) are also shown (solid blue curve).

like bubbles in their slowing-down phase. A representative sample of such simulations, including our fiducial setup J2 and its variants J2a through J2d, are summarised in the right columns of Table 3, and are depicted in Figure 12. The observed height and width of the FBs strongly constrain the initial conditions of the simulations, such that large deviations from the J1 or J2 parameters generally yield simulated bubbles inconsistent with observations.

By separately varying each of the J2a setup parameters, one at a time, we derive the functional dependencies of the bubble age in the close vicinity of the J2a setup,

$$\mathbb{T} \simeq 1.81 \left(\frac{E_j}{3 \times 10^{55} \text{ erg}} \right)^{-1.51 \pm 0.06} \beta_{-1}^{1.92 \pm 0.10} \mu_{10}^{1.58 \pm 0.06} \times t_{0.04}^{0.55 \pm 0.05} \text{ Myr}, \quad (50)$$

maximal half-width,

$$R_{\max} \simeq 1.95 \left(\frac{E_j}{3 \times 10^{55} \text{ erg}} \right)^{-0.77 \pm 0.05} \beta_{-1}^{1.13 \pm 0.07} \mu_{10}^{1.2 \pm 0.1} \times t_{0.04}^{0.37 \pm 0.03} \text{ kpc}, \quad (51)$$

maximal longitude,

$$\Delta l \simeq 13^\circ .1 \left(\frac{E_j}{3 \times 10^{55} \text{ erg}} \right)^{-0.79 \pm 0.05} \beta_{-1}^{1.26 \pm 0.08} \mu_{10}^{1.13 \pm 0.07} \times t_{0.04}^{0.37 \pm 0.04}, \quad (52)$$

and Mach number of the head,

$$\Upsilon \simeq 3.73 \left(\frac{E_j}{3 \times 10^{55} \text{ erg}} \right)^{1.27 \pm 0.13} \beta_{-1}^{-1.14 \pm 0.14} \mu_{10}^{-1.0 \pm 0.1} \times t_{0.04}^{-0.40 \pm 0.05}. \quad (53)$$

These individual parametric scans are illustrated in Figure 13. Notice that the energy-dependencies in the top row are not well-fit by a power law.

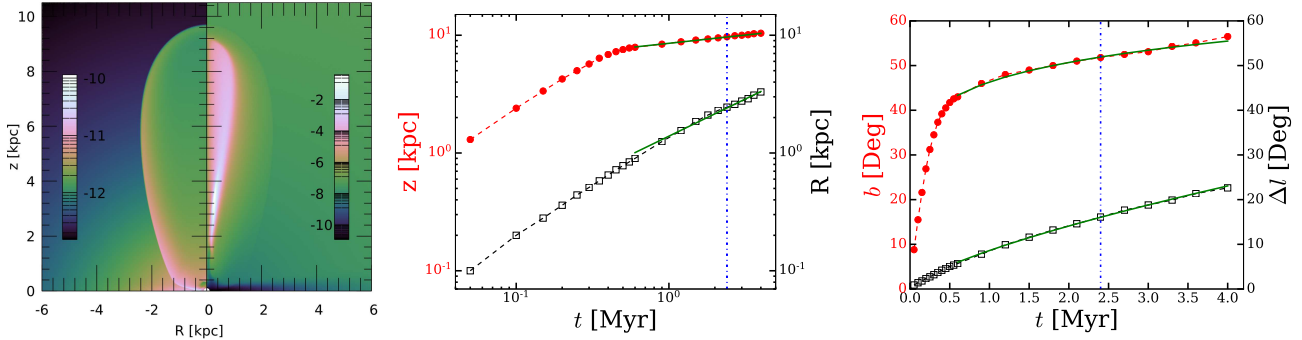


Figure 11. Same as Figure 8, but for our fiducial slowdown bubble (setup J2).

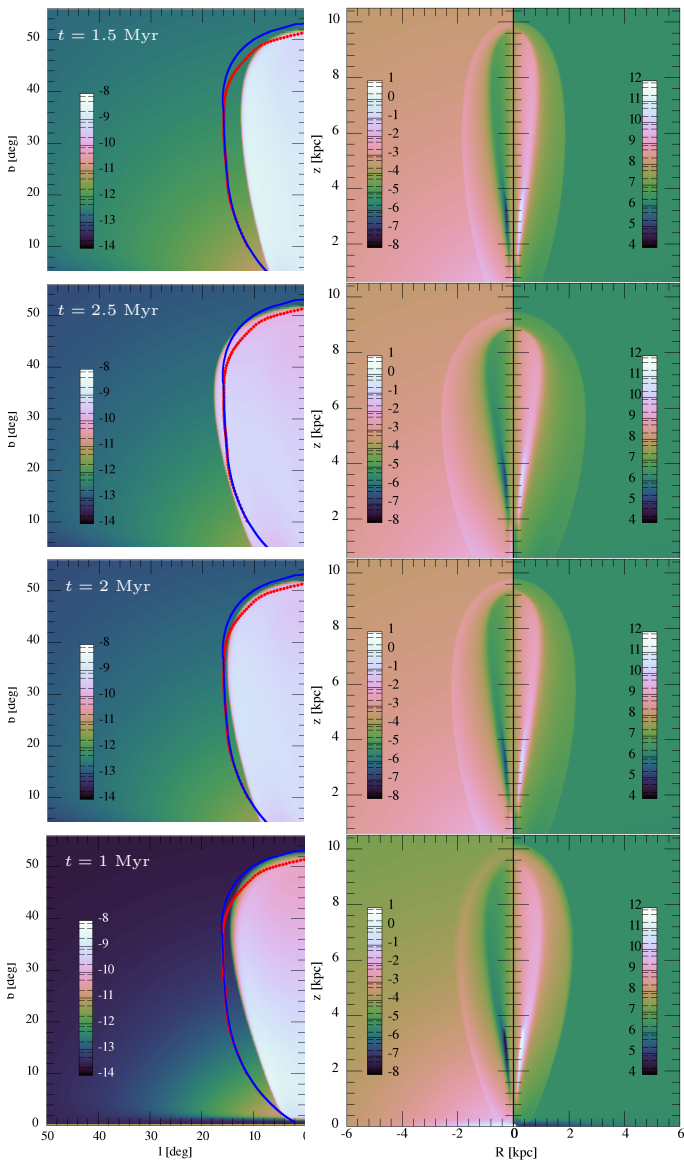


Figure 12. Variations on the slowing-down bubble setup J2a (top row), which itself is identical to J2 but with $E_j = 3 \times 10^{55}$ erg. Single-parameter variations include $\beta_j = 0.12$ (J2b, second row), $t_j = 0.06$ Myr (J2c, third row), and $M_d = 1.2 \times 10^{11} M_\odot$ (J2d, fourth row). Notations are the same as in Figure 2.

These results are generally consistent with our model, considering the limited dynamical range explored. For $z_s \simeq 8$ kpc and $\tau_z = 0.14$, the age of the bubble in Eq. (31) scales approximately as $\mathbb{T} \propto v_k^{-1} z_s^{-2.2}$. Combining this with Eqs. (41) and (42) yields $\mathbb{T} \propto E_j^{-1.5} \beta_j^{1.9} \mu_{\max}^{1.5}$, in qualitative agreement with the fit (50). Equation (40) then gives $R_{\max} \propto E_j^{-0.7} \beta_j^{1.5} \mu_{\max}^{1.0}$, in fairly good agreement with the fit (51). Taking the time derivative of Eq. (30) yields, for late-times when $z_H(t)$ is a power-law, $\Upsilon \simeq (\tau_z z_H) / (\mathbb{T} c_s) \propto \mathbb{T}^{-1}$, in qualitative agreement with the fit (53). Taking into account corrections to $z_H(t)$ gives $\Upsilon \simeq (v_k/c_s)(z_H/z_s)^{1-\tau_z} \propto v_k \mathbb{T}^{-1.2} \propto E_j^{1.8} \beta_j^{-1.3} \mu_{\max}^{-1.8}$, partly consistent with (53). Some positive dependence of θ_{eff} upon the injection time is expected in (42); the t_j dependence of the fits (50)–(53) would match the model if $\theta_k \propto t_j^{0.2}$.

The slowing-down bubbles are more sensitive to the Galactic model than their ballistic counterparts. Increasing the disc mass significantly lowers both the age and the width of the slowing-down bubble, as it leads to a steeper, $\alpha > 2$ CGM density profile. This effect, along with the slower sideways expansion inside the disc, lead to younger bubbles more pinched at their base, as seen in the bottom panel of Figure 12. Other parameters have a more modest effect. Introducing extreme CGM rotation, for example, renders the bubbles slightly thinner, but does not substantially modify their age, as shown in the bottom panel of the figure.

5 SUMMARY AND DISCUSSION

We model the FBs under the assumption that their edges are strong forward shocks, as based on recent evidence (§1). We simulate a bubble in one Galactic hemisphere as either an undirected release of energy near or above the GC (§3) or as a collimated injection of both energy and momentum as a jet emanating from CBH on ~ 100 pc scales (§4). The evolved FBs, computed for various injection and CGM parameters, are compared to observations in order to constrain both the FB engine and the Galactic model. The study combines analytic modeling with converged (§B) axisymmetric hydrodynamic PLUTO-v4.0 simulations (§2), which implement various hydrostatic models of the Galaxy (§A) including halo, disc, and bulge components.

A putative non-directed FB engine, injecting energy but not momentum, leads to a fairly spherical bubble due to the fast sideways expansion after the bubble emerges from the

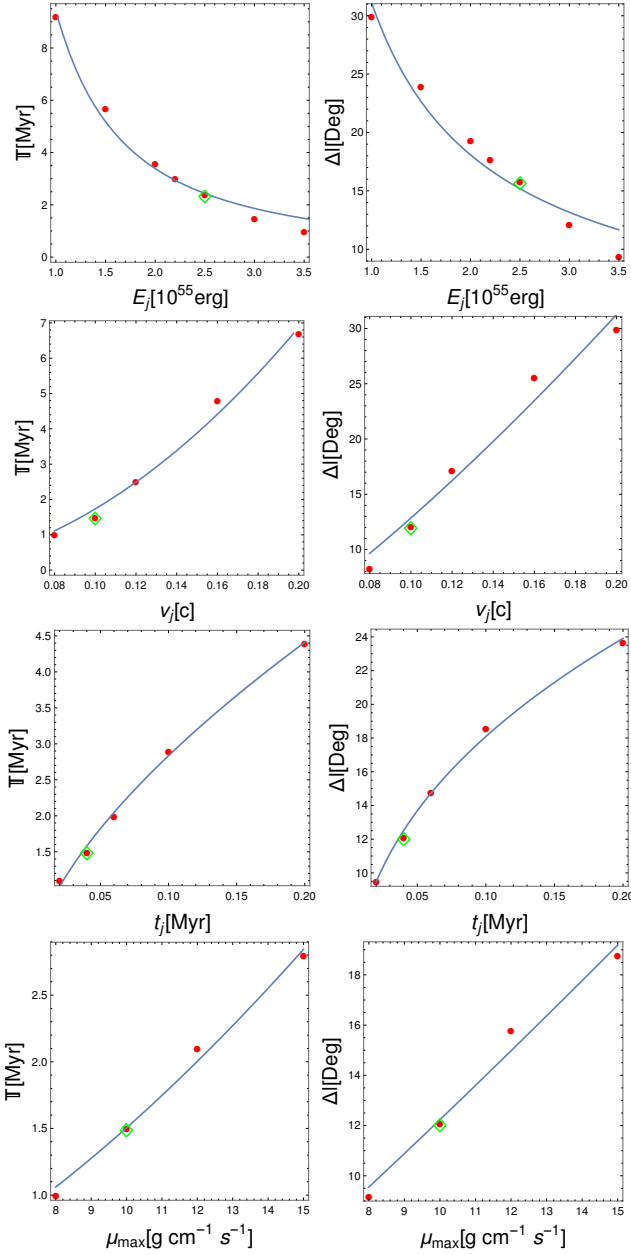


Figure 13. The profiles of \mathbb{T} (right panel) and Δl (left panel) for a range of E_j (first row), v_j (second row), t_j (third row), and μ_{\max} (fourth row). The red filled circles are the simulated results, fitted with power-law functions (blue solid lines). For \mathbb{T} (E_j) dependence, β_j and t_j are kept set at 0.1 and 0.04 Myr. During other parameters dependence test we kept E_j set at 3×10^{55} erg. The θ_j parameter was set to 4° for all dependencies test. The green diamonds show the best fitted parameters for the setup J2.

disc. The evolution is characterised by a $\lesssim 1$ Myr linear, ballistic stage followed by an approximately self-similar, sublinear, spherical evolution. By the time the top of the bubble reaches the $|b| \simeq 52^\circ$ latitude of the FBs, it is too spherical to agree with observations, whether the engine is placed in the Galactic centre or is effectively offset to intermediate, order $z \sim 1$ kpc heights (Figure 2). This conclusion remains valid for a wide range of Galactic models (Figure 3 and Figure 4), including extreme variations in Galactic disc

and bulge masses, fast and even maximal CGM halo rotation, and combining the above effects; see Table 2. We conclude that a non-directed engine fails to generate FBs with forward shock edges consistent with observations for any plausible Galactic model.

In contrast, an outflow collimated into a thin jet, launched near the GC approximately perpendicular to the disc, can reproduce the observed morphology of the FB edge as a strong forward shock. The evolution can be crudely understood using a stratified model (§4.1), in which the gas behind the head of the jet is approximated as expanding sideways at a fixed z , as verified by numerical simulations (§4.2). The bubble initially evolves ballistically, $z_H \propto t$, until it accumulates sufficient mass and starts slowing down, with momentum conservation leading to a very slow, $z_H \propto t^{(0.1-0.2)}$ subsequent growth (Equation 28). As the transition height $z_s \gtrsim 5$ kpc (Figure 6) can be above or below the present-day $z_H \simeq 10$ kpc tip of the bubble, the FBs can be either in the ballistic phase (large E/β_j ; Equation 11) or in the slowdown phase (small E/β_j ; Equation 12). In both regimes, we identify plausible injection parameters (Table 3) that yield bubbles (modeled: left panel of Figure 5; simulated: Figure 7) consistent with the observed edges (KG17) and X-ray shell (KG18) of the FBs.

If the injection is sufficiently energetic or the jet is slow, $E_{55} \gtrsim 3(\beta_{-2}\theta_5)^2$, then the FBs are still ballistic. A high Mach number Υ at the top of the bubble then requires $\beta_{-2} \simeq 0.35\Upsilon_5$, and the thickness of the bubbles requires $\theta_k \simeq 4^\circ$. The injected energy (both hemispheres) is then $E_{55} \gtrsim 2\beta_{-2}^2 \gtrsim 0.2\Upsilon_5^2$ and the age of the bubbles is $\mathbb{T} \simeq 3.3\beta_{-2}^{-1} \text{ Myr} \lesssim 8\Upsilon_5^{-1} \text{ Myr}$. Our simulations show bubbles broadly consistent with the model in terms of structure (Figure 5 and the top panel of Figure 7), evolution (Figure 8), and parameter dependence (Figure 9 and Figure 10). We identify a pronounced low-pressure region behind the head of the simulated ballistic bubble, consisting of unperturbed jet material. The ballistic nature of the bubble renders it nearly independent of the Galactic model.

In contrast, if the injection is sufficiently fast or of low energy, E/β_k is small (Equation 12) and the observed FBs are already in their slowdown phase. The injected energy is then $E_{55} \lesssim 3(\beta_{-2}\theta_5)^2$, in which case $0.05\Upsilon_5^2\theta_5^2 \lesssim E_{55} \lesssim 2\beta_{-2}^2$ and $\mathbb{T} \simeq 1.4(\beta_{-2}\theta_5)^{-1} \text{ Myr} \lesssim 4(\Upsilon_5\theta_5)^{-1} \text{ Myr}$. Such slowing-down FBs can still be energetic, provided that β_{-2} is large, but their age would then be of order a Myr only if θ_5 is small. Our simulations again show bubbles broadly consistent with the model in terms of structure (bottom panel of Figure 7), evolution (Figure 11), and parameter dependence (Figure 12 and Figure 13). These bubbles have a more regular inner structure, without the aforementioned low-pressure region. The edges of the bubbles in the slowdown phase are somewhat dependent on the disc mass.

While the FB edges and X-ray shell can be reproduced equally well if observed in the ballistic or slowdown phases, the evolution of the inner structure of the bubble can distinguish between the phases. The ballistic FB shows an inner cylindrical shock surrounded at its top by an irregular contact discontinuity surface, whereas the slowing-down FB shows a bubble-like contact discontinuity trailing the shock. The high, $\Upsilon \gtrsim 5$ Mach number of the forward shock, inferred from observations (KG17; KG18), is consistent with

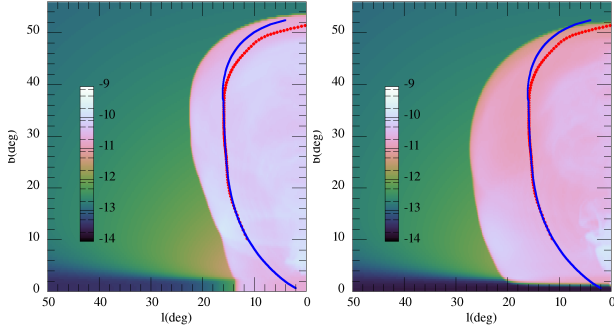


Figure 14. Simulated FBs generated using the setup of ZG20 with their injection above the disc ($r_0 = 0.35$ kpc; left panel; at $T = 5.0$ Myr) and for the same parameters but injection inside the disc ($r_0 = 0.05$ kpc; right panel; at $T = 7.5$ Myr). Notations are the same as in Figure 2. In both cases, the FBs are too wide and the shocks too weak to match observations.

both ballistic and early slowdown phases, and is one of several indications that $z_s \gtrsim 5$ kpc.

The temperature behind the shock is a useful diagnostic of the FB energetics, being directly related to the shock velocity and insensitive to high-energy processes. The (1–2) keV temperatures in our nominal simulations are slightly higher than the 0.4 – 0.5 keV electron temperatures estimated based on the O VII and O VIII line ratios (Miller & Bregman 2016) and on the X-ray shell (KG18). The difference is consistent with a partial equilibration of electrons at the high-Mach shock, as the Coulomb equilibration timescale (Spitzer 1956),

$$t_{eq} \simeq 7.9 \left(\frac{T}{10^7 \text{ K}} \right)^{3/2} \left(\frac{n}{10^{-3} \text{ cm}^{-3}} \right)^{-1} \text{ Myr}, \quad (54)$$

is longer than the ~ 2 –3 Myr age of our simulated FBs. A time-dependent calculation of the energy transfer between electrons and protons (see appendix B of Sarkar et al. 2017) indicates that by ~ 3 Myr, the electron temperature reaches $\sim 4 \times 10^6$ K, consistent with observations.

During the course of this work, ZG20 presented simulated FBs with forward shock edges from jet injection, considering a much narrower parameter range than studied here. The preferred (case A) ZG20 scenario is roughly comparable to our directed injection with slowing-down FBs, based on its parameters ($E \simeq 2.2 \times 10^{55}$ erg and $\beta_j \simeq 0.08$) and declining shock Mach number. However, the resulting FBs are not fully consistent with observations, as the simulated FBs are too wide (reaching $R \simeq 3.5$ kpc) and the shocks are too weak (with $\Upsilon \simeq 2.2$ at z_H and $\Upsilon < 1.5$ below $z_H/2$); indeed, the combination of thin FBs and a high Mach number imposes strong constraints on the injection setup. Moreover, the ZG20 injection appears unrealistically long, with $t_j = 1.0$ Myr, and is deposited at a height $r_0 \simeq 350$ pc, avoiding the propagation of the jet through the disc. Figure 14 shows that while the ZG20 setup already leads to FBs too wide, incorporating the disc component exacerbates the discrepancy.

We have shown that FB observations identifying the edges as forward shocks imply a collimated injection, which we model as $\theta \lesssim 4^\circ$ jets along the Galactic z axis as they emerge on ~ 100 pc scales. Sufficiently small inclinations with respect to the z axis, of order $\theta \lesssim 30^\circ$, say, may still

provide a good match to the FBs, but we could not explain forward-shock FB edges with jets of large inclinations. It is generally believed that highly collimated jets are launched by a rapidly spinning CBH along the spin axis (e.g., McKinney et al. 2013). While a jet perpendicular to the Galactic plane does not seem consistent with the presently inferred spin orientation (e.g., Gravity Collaboration et al. 2018), rapid changes in spin direction may be natural for such a CBH (e.g., Dotti et al. 2012). Therefore, our results impose a challenge on modeling the launching of the jet and its collimation on small scales.

ACKNOWLEDGEMENTS

We thank P. Sharma, C. M. Irwin, B. Nath, and T. Piran for useful discussions. This research has received funding from the IAEC-UPBC joint research foundation (grant No. 300/18), the GIF (Grant No. I-1362-303.7/2016), and the Israel Science Foundation (ISF grant No. 1769/15), and was supported by the Ministry of Science, Technology & Space, Israel. KCS was supported by the Israeli Centers of Excellence (I-CORE) program (center No. 1829/12) and the Israeli Science Foundation (ISF grant No. 2190/20).

REFERENCES

- Arnaud M., Rothenflug R., 1985, *A&AS*, **60**, 425
 Ashley T., Fox A. J., Jenkins E. B., Wakker B. P., Bordoloi R., Lockman F. J., Savage B. D., Karim T., 2020, *ApJ*, **898**, 128
 Baganoff F. K., et al., 2003, *ApJ*, **591**, 891
 Bland-Hawthorn J., Cohen M., 2003, *ApJ*, **582**, 246
 Bland-Hawthorn J., et al., 2019, *ApJ*, **886**, 45
 Bordoloi R., et al., 2017, *ApJ*, **834**, 191
 Braginskii S. I., 1958, *Soviet Journal of Experimental and Theoretical Physics*, **6**, 358
 Carretti E., et al., 2013, *Nature*, **493**, 66
 Chandrasekhar S., 1961, *Hydrodynamic and Hydromagnetic Stability*. International series of monographs on physics, Clarendon Press, <https://books.google.co.il/books?id=XvZ0tgEACAAJ>
 Cheng K.-S., Chernyshov D. O., Dogiel V. A., Ko C.-M., Ip W.-H., 2011, *ApJ*, **731**, L17
 Crocker R. M., 2012, *MNRAS*, **423**, 3512
 Dobler G., 2012, *ApJ*, **760**, L8
 Dobler G., Finkbeiner D. P., 2008, *ApJ*, **680**, 1222
 Dobler G., Finkbeiner D. P., Cholis I., Slatyer T., Weiner N., 2010, *ApJ*, **717**, 825
 Dotti M., Colpi M., Pallini S., Perego A., Volonteri M., 2012, *The Astrophysical Journal*, **762**, 68
 Fox A. J., et al., 2015, *ApJ*, **799**, L7
 Fujita Y., Ohira Y., Yamazaki R., 2013, *ApJ*, **775**, L20
 Gravity Collaboration et al., 2018, *A&A*, **618**, L10
 Guo F., Mathews W. G., 2012, *ApJ*, **756**, 181
 Heywood I., et al., 2019, *Nature*, **573**, 235
 Irwin C. M., Nakar E., Piran T., 2019, *MNRAS*, **489**, 2844
 Karim M. T., et al., 2018, *ApJ*, **860**, 98
 Kataoka J., et al., 2013, preprint, ([arXiv:1310.3553](https://arxiv.org/abs/1310.3553))
 Kataoka J., Yamamoto M., Nakamura Y., Ito S., Sofue Y., Inoue Y., Nakamori T., Totani T., 2021, *ApJ*, **908**, 14
 Keshet U., Gurwicz I., 2017, *ApJ*, **840**, 7
 Keshet U., Gurwicz I., 2018, *MNRAS*, **480**, 223
 Lacki B. C., 2014, *MNRAS*, **444**, L39
 Lamb H., 1932, *Hydrodynamics*. The University Press, <https://books.google.co.il/books?id=BfZQAAAAMAAJ>

- Liedahl D. A., Osterheld A. L., Goldstein W. H., 1995, *ApJ*, **438**, L115
- McKinney J. C., Tchekhovskoy A., Blandford R. D., 2013, *Science*, **339**, 49
- Mewe R., Gronenschild E. H. B. M., van den Oord G. H. J., 1985, *A&AS*, **62**, 197
- Mewe R., Lemen J. R., van den Oord G. H. J., 1986, *A&AS*, **65**, 511
- Mignone A., Bodo G., Massaglia S., Matsakos T., Tesileanu O., Zanni C., Ferrari A., 2007, *ApJS*, **170**, 228
- Miller M. J., Bregman J. N., 2016, *ApJ*, **829**, 9
- Miyamoto M., Nagai R., 1975, *PASJ*, **27**, 533
- Mou G., Yuan F., Bu D., Sun M., Su M., 2014, *ApJ*, **790**, 109
- Mou G., Yuan F., Gan Z., Sun M., 2015, *ApJ*, **811**, 37
- Navarro J. F., Frenk C. S., White S. D. M., 1996, *ApJ*, **462**, 563
- Planck Collaboration 2013, *A&A*, **554**, A139
- Ponti G., et al., 2019, *Nature*, **567**, 347
- Roediger E., Kraft R. P., Nulsen P., Churazov E., Forman W., Brügggen M., Kokotanekova R., 2013, *MNRAS*, **436**, 1721
- Sarkar K. C., Nath B. B., Sharma P., Shchekinov Y., 2015a, *MNRAS*, **448**, 328
- Sarkar K. C., Nath B. B., Sharma P., 2015b, *MNRAS*, **453**, 3827
- Sarkar K. C., Nath B. B., Sharma P., 2017, *MNRAS*, **467**, 3544
- Sofue Y., 2000, *ApJ*, **540**, 224
- Spitzer L., 1956, *Physics of Fully Ionized Gases*. Interscience tracts on physics and astronomy, Interscience Publishers, <https://books.google.co.il/books?id=uWYFAAAAMAAJ>
- Spitzer L., 1962, *Physics of Fully Ionized Gases*. Interscience tracts on physics and astronomy, Interscience Publishers, <https://books.google.co.il/books?id=CilRAAAAMAAJ>
- Su M., Slatyer T. R., Finkbeiner D. P., 2010, *ApJ*, **724**, 1044
- Veilleux S., Cecil G., Bland-Hawthorn J., 2005, *ARA&A*, **43**, 769
- Zhang R., Guo F., 2020, *ApJ*, **894**, 117
- Zubovas K., Nayakshin S., 2012, *MNRAS*, **424**, 666

APPENDIX A: GALACTIC MODEL

The galactic model implemented in the simulations contains gas components which are in a steady state equilibrium with a static gravitational potential. The potential consists of a cylindrically symmetric stellar disc and spherically symmetric stellar bulge and dark matter components. For the stellar disc, we use a Miyamoto & Nagai (1975) potential in a cylindrical form,

$$\Phi_d = -\frac{GM_d}{\sqrt{R^2 + (a_d + \sqrt{z^2 + b_d^2})^2}}, \quad (\text{A1})$$

where $a_d \geq 0$ and $b_d \geq 0$ represent the scale length and scale height of the stellar disc of mass M_d . For the dark matter, we use a modified form of the NFW potential (Navarro et al. 1996) to include a core that produces a finite dark matter (DM) density at the centre,

$$\Phi_{\text{DM}} = -\frac{GM_{\text{vir}}}{f(c_{\text{vir}})} \frac{\ln\left(1 + \sqrt{\frac{r^2 + d^2}{r_s^2}}\right)}{\sqrt{r^2 + d^2}},$$

where $c_{\text{vir}} = r_{\text{vir}}/r_s$ is the DM concentration parameter, $f(c_{\text{vir}}) = \log(1 + c_{\text{vir}}) - c_{\text{vir}}/(1 + c_{\text{vir}})$, r_{vir} and r_s are respectively the virial radius and scale radius for a DM halo of mass M_{vir} , and d is the core radius of the DM distribution. The bulge potential is considered to have the form

$$\Phi_b = -\frac{GM_b}{\sqrt{r^2 + a_b^2}}, \quad (\text{A2})$$

where a_b is the scale radius and M_b is the mass of the stellar bulge. Thus the total Galactic potential becomes

$$\Phi(R, z) = \Phi_d(R, z) + \Phi_b(R, z) + \Phi_{\text{DM}}(R, z). \quad (\text{A3})$$

For the gaseous components, we consider a circumgalactic medium (halo), an ISM disc, and a central molecular zone (CMZ) component. Each of these components follows an independent steady-state equilibrium with the total gravitational potential $\Phi(R, z)$. For example, the density distribution of the ISM disc component, in equilibrium, can be written as (for a derivation, see Sarkar et al. 2015a)

$$\frac{\rho_d(R, z)}{\rho_{d0}} = \exp\left\{-\frac{\Phi(R, z) - \Phi_0 - [\Phi(R, 0) - \Phi_0]f_d^2}{c_{\text{sd}}^2}\right\}, \quad (\text{A4})$$

where the potential $\Phi_0 \equiv \Phi(0, 0)$ and ISM disc mass-density $\rho_{d0} \equiv \rho_d(0, 0)$ are evaluated at the Galactic centre, $c_{\text{sd}} \equiv c_{\text{sd}}(T_{\text{sd}}) = (k_B T_{\text{sd}}/\mu_m m_p)^{1/2}$ is the isothermal sound speed (including turbulence) of the disc gas, and f_d is the rotation velocity ratio between the disc gas $v_{\phi, d}(R)$ and stellar component $v_{\phi, G}(R) = (-R \partial\Phi/\partial R|_{z=0})^{1/2}$ at any given cylindrical radius R . We assume this ratio and the sound speed to be independent of R and z , in order to obtain an analytical expression for the density distribution.

We obtain the density distributions of the other components in a similar way. For the halo and the CMZ, the density distributions are, respectively,

$$\frac{\rho_h(R, z)}{\rho_{h0}} = \exp\left\{-\frac{\Phi(R, z) - \Phi_0 - [\Phi(R, 0) - \Phi_0]f_h^2}{c_{\text{sh}}^2}\right\}, \quad (\text{A5})$$

and

$$\frac{\rho_{\text{cmz}}(R, z)}{\rho_{\text{cmz}0}} = \exp\left\{-\frac{\Phi(R, z) - \Phi_0 - [\Phi(R, 0) - \Phi_0]f_{\text{cmz}}^2}{c_{\text{scmz}}^2}\right\}, \quad (\text{A6})$$

where, $\rho_{h0} \equiv \rho_h(0, 0)$, $\rho_{\text{cmz}0} \equiv \rho_{\text{cmz}}(0, 0)$, and rotation factors f are defined analogously to f_d in Eq. (A4).

The total density at any computational cell is therefore given as $\rho_{\text{tot}}(R, z) = \rho_d(R, z) + \rho_h(R, z) + \rho_{\text{cmz}}(R, z)$. Since each of these components may have a different rotation speed, the effective rotation speed $v_{\phi, \text{eff}}$ at any computational cell is given by

$$\frac{v_{\phi, \text{eff}}(R, z)}{v_{\phi, G}(R)} = \sqrt{\frac{f_d^2 \rho_d(R, z) + f_h^2 \rho_h(R, z) + f_{\text{cmz}}^2 \rho_{\text{cmz}}(R, z)}{\rho_{\text{tot}}(R, z)}}. \quad (\text{A7})$$

Notice that, although we include the CMZ component, it is set to zero in practice in the simulations shown.

APPENDIX B: CONVERGENCE TESTS

Figure B1 shows the contemporary projected FB images obtained for non-directed, GC injection (setup S1) for stretched $\{r, \theta\}$ grids of dimensions $\{1024 \times 256\}$ (left) and $\{2048 \times 512\}$ (right). The two images are sufficiently similar to warrant adopting $\{1024 \times 256\}$ as the base resolution for non-directed simulations.

For directed injection, we find that a higher resolution is

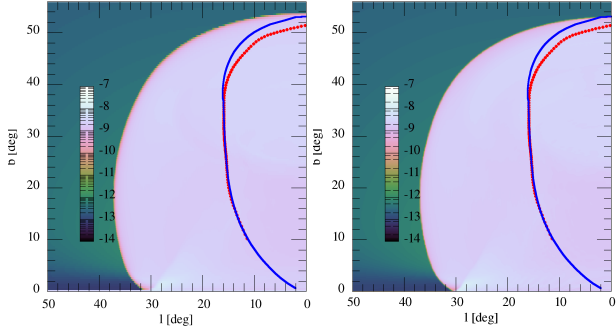


Figure B1. Same as top panel of [Figure 2](#) (setup S1), but for simulation grids 1024×256 (left) and 2048×512 (right) in the $\{r, \theta\}$ directions.

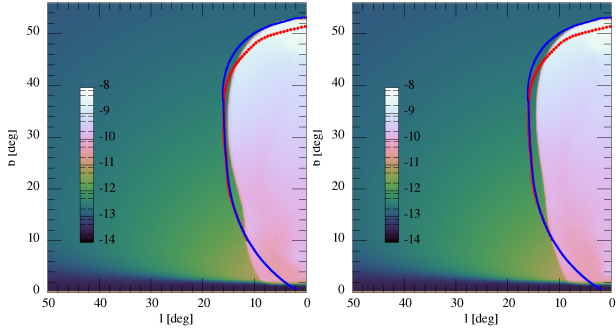


Figure B2. Same as top panel of [Figure 7](#) (setup J1), but for $\theta_j = 4^\circ$, with simulation grids $\{1024 \times 512\}$ (left) and $\{2048 \times 1024\}$ (right).

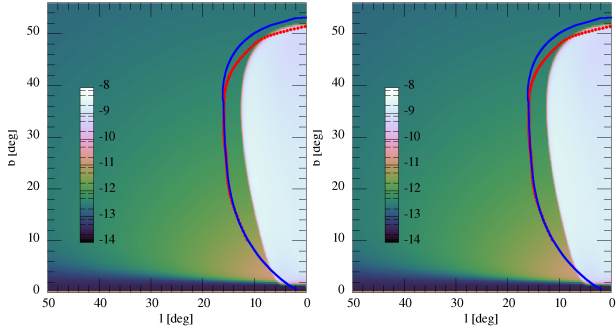


Figure B3. Same as top panel of [Figure 12](#) (setup J2a) but for simulation grids $\{1536 \times 768\}$ (left) and $\{3072 \times 1536\}$ (right).

needed to guarantee convergence. In the ballistic case, shown in [Figure B2](#), we find that $\{1024 \times 512\}$ suffices as our base resolution. In the slowdown regime, shown in [Figure B3](#), a base resolution $\{1536 \times 768\}$ is sufficient.

This paper has been typeset from a $\text{\TeX}/\text{\LaTeX}$ file prepared by the author.